Marine and Petroleum Geology 133 (2021) 105195

Contents lists available at ScienceDirect

Marine and Petroleum Geology

journal homepage: www.elsevier.com/locate/marpetgeo

# How initial basin geometry influences gravity-driven salt tectonics: Insights from laboratory experiments

Frank Zwaan [a,b,c,*], Matthias Rosenau [d], Daniele Maestrelli [e]

[a] Géosciences Rennes, Unité Mixte de Recherche, 6118, CNRS et Université de Rennes 1, 35042, Rennes, France
[b] Dipartimento di Scienze della Terra, Università degli Studi di Firenze, Via G. La Pira 4, 50121, Florence, Italy
[c] Institute of Geological Sciences, University of Bern, Baltzerstrasse 1 + 3, 3012, Bern, Switzerland
[d] Helmholtz Centre Potsdam - GFZ German Research Centre for Geosciences, Telegrafenberg, Potsdam, 14473, Germany
[e] Consiglio Nazionale delle Ricerche, Istituto di Geoscienze e Georisorse (CNR-IGG), Via G. La Pira 4, 50121, Florence, Italy

ARTICLE INFO

*Keywords:*
Salt tectonics
Margin tilting
Salt basin geometry
Analogue modelling
Gravity gliding

ABSTRACT

As a rifted margin starts to tilt due to thermal subsidence, evaporitic bodies can become unstable, initiating gravity-driven salt tectonics. Our understanding of such processes has greatly benefitted from tectonic modelling efforts, however a topic that has gotten limited attention so far is the influence of large-scale salt basin geometry on subsequent salt tectonics. The aim of this work is therefore to systematically test how salt basin geometry (initial salt basin depocenter location, i.e. where salt is thickest, as well as mean salt thickness) influence salt tectonic systems by means of analogue experiments. These experiments were analyzed qualitatively using top view photography, and quantitatively through Particle Image Velocimetry (PIV), and 3D photogrammetry (Structure-from-Motion, SfM) to obtain their surface displacement and topographic evolution. The model results show that the degree of (instantaneous) margin basin tilt, followed by the mean salt thickness are dominant factors controlling deformation, as enhancing basin tilt and/or mean salt thickness promotes deformation. Focusing on experiments with constant basin tilt and mean salt thickness to filter out these dominant factors, we find that the initial salt depocenter location has various effects on the distribution and expression of tectonic domains. Most importantly, a more upslope depocenter leads to increased downslope displacement of material, and more subsidence (localized accommodation space generation) in the upslope domain when compared to a setting involving a depocenter situated farther downslope. A significant factor in these differences is the basal drag associated with locally thinner salt layers. When comparing our results with natural examples, we find a fair correlation expressed in the links between salt depocenter location and post-salt depositional patterns: the subsidence distribution due to the specific salt depocenter location creates accommodation space for subsequent sedimentation. These correlations are applicable when interpreting the early stages of salt tectonics, when sedimentary loading has not become dominant yet.

## 1. Introduction

The deposition of extensive evaporite (salt) deposits is a common occurrence during and after continental break-up and the associated marine transgressions. Examples of such evaporite deposits are found at numerous passive margins around the world (e.g. Hudec and Jackson, 2006, 2012; Brun and Fort, 2011; Tari and Jabour, 2013; Rowan, 2014, 2018; Warren, 2016, Jackson & Hudec 2017), whereas rift-related deposition of evaporites is on-going in the Afar rift in East Africa (Bonatti et al., 1971). As the margin starts tilting due to thermal subsidence of the adjacent oceanic basin (Fig. 1b), sufficiently large evaporitic bodies can become gravitationally unstable, initiating gravity gliding-type salt tectonics in which post-salt sediments are detached from the pre-salt substratum and transported downslope (e.g. at the Angolan and Brazilian margins of the South Atlantic, Marton et al., 2000; Fort et al., 2004a; Quirk et al., 2012; Jackson et al., 2015). Typical of such salt tectonic systems is the development of upslope extensional structures including rotated blocks and rollovers, a mid-slope translational domain and a downslope compressional domain with diapirs, folding and faulting (e.g. Demercian et al., 1993; Spathopolous, 1996; Rowan et al., 2004; Brun and Fort, 2011, Fig. 1c). In some cases, the evaporites can even pierce the sedimentary cover and extrude

* Corresponding author. Institute of Geological Sciences, University of Bern, Baltzerstrasse 1 + 3, 3012, Bern, Switzerland.
*E-mail address:* frank.zwaan@geo.unibe.ch (F. Zwaan).

https://doi.org/10.1016/j.marpetgeo.2021.105195
Received 15 October 2020; Received in revised form 15 April 2021; Accepted 16 June 2021
Available online 8 July 2021

downslope over the exposed seafloor (e.g. Rowan et al., 2004; Hudec and Jackson, 2006; Tari and Jabour, 2013). Within this context, it must be stressed that next to margin tilt, sedimentary loading can have an important influence on the development of salt tectonic systems and the relative significance of both driving forces remains debated (e.g. Schultz-Ela, 2001; Brun and Fort, 2011, 2012; Rowan et al., 2012; Goteti et al., 2013; Peel, 2014; Warren, 2016).

Evaporite units and associated salt tectonic structures are notoriously challenging to interpret and reconstruct on seismic lines, and our understanding of salt tectonic processes has greatly benefitted from analogue and numerical modelling efforts (e.g. Cobbold and Szatmari, 1991; Gaullier et al., 1993; Vendeville et al., 1995; Mauduit and Brun, 1998; Fort et al., 2004a, Gemmer et al., 2004; Ings et al., 2004; Gaullier and Vendeville, 2005; Peel, 2014; Brun and Fort, 2004, 2011; Quirk et al., 2012; Goteti et al., 2013; Allen and Baumont, 2012, 2015; Ferrer et al., 2017; Ge et al., 2019a,b; Pichel et al., 2018, 2019). Such studies provided insights into the structural evolution of the various domains within gravity gliding systems, for instance showing how deformation may migrate up- and downslope over time (Fort et al., 2004a, Brun and Fort, 2004, 2011; Quirk et al., 2012; Ge et al., 2019a, b). Also the

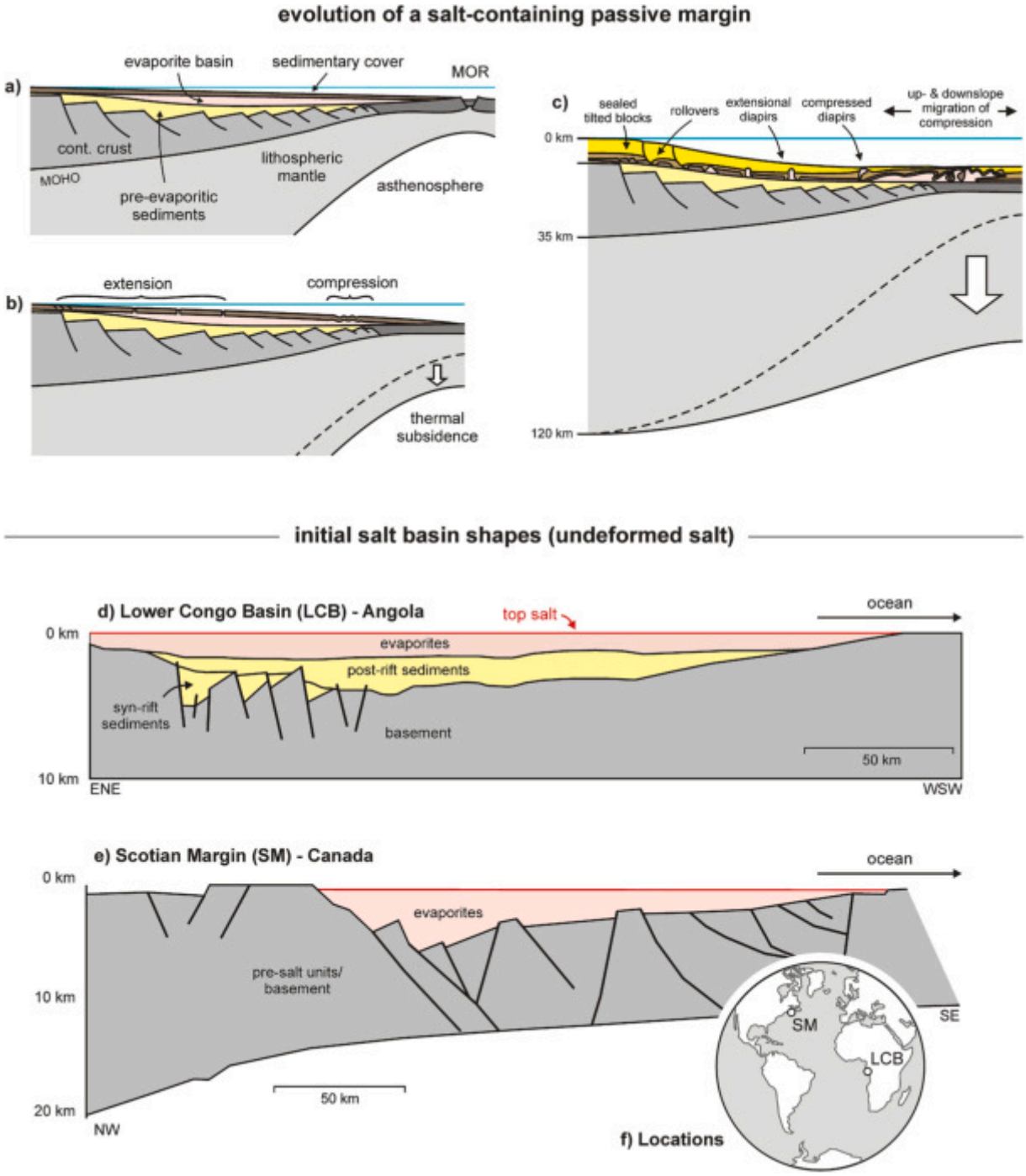


**Fig. 1.** (a–c) Generalized tectonic evolution of a passive margin containing evaporite deposits undergoing differential thermal subsidence and oceanward tilting. Image modified after Fort et al. (2004a) and reproduced with permission from the AAPG. (d–g) Reconstructions of undeformed evaporite basins in presently tilted passive margins within the Atlantic realm. (d) Lower Congo Basin, offshore Angola, with an evaporite depocenter downslope (i.e. towards the ocean). Image modified after Marton et al. (2000). (e) Section NS 2000 across the Scotian Margin, offshore eastern Canada, with a main evaporite basin depocenter upslope. Image modified after PFA (2011). (f) Locations of natural examples (d–g). LCB: Lower Congo Basin, MOHO: Mohorovičić discontinuity, MOR: mid-oceanic ridge, SM: Scotian Margin.

interaction between (syn-kinematic) sedimentation and salt tectonics has received much attention. Fort et al. (2004b) for instance demonstrated how differential sedimentation along a margin can cause downslope velocity differences resulting in block rotation about a vertical axis. Recently, Goteti et al. (2013) and Ge et al. (2019a) have experimented with varying sedimentation patterns, finding that differential sedimentation may lead to the widespread formation of minibasins, thus preventing the development of a well-defined translational domain. Next to the influence of sedimentation, the effects of different margin inclination histories (i.e. instant vs. progressive tilting) have been investigated as well, showing that faster margin tilting enhances (initial) downward displacement (e.g. Goteti et al., 2013) and causes more distributed deformation (Ge et al., 2019b).

A factor that has however gotten only limited attention until recently is the effect of salt layer thickness variations due to different basin geometries during initial salt deposition. Such variations may be due to the characteristics of the margin: a wide rifted margin would allow for extensive salt deposits, whereas a narrow margin provides only limited space. Also the thermal profile of the lithosphere may influence salt deposition patterns, given that salt is often accumulated during the later stages of continental break-up and the onset of thermal sag (e.g. Rowan, 2018, and references therein). Another process affecting these systems is pre-salt sedimentation, which may smoothen the base of the salt basin by covering the otherwise rough bathymetry created by syn-rift faulting (e.g. Strozyk et al., 2017, Fig. 1d). However, when syn-rift salt deposition occurs, active faulting may cause the development of smaller and isolated salt basins with limited potential for salt-tectonic deformation (Brun & Fort 2008, 2011; Tari and Jabour, 2013; Rowan, 2014, Jackson & Hudec 2017). Salt basins can thus exhibit a high degree of geometric variability (e.g. Peel et al., 1995; Marton et al., 2000, PFA , 2011; Zalán et al., 2011; Davison et al., 2012; Guerra and Underhill, 2012; Garcia et al., 2012; Tari and Jabour, 2013; Strozyk et al., 2017, Fig. 1d and e), and such variations, which can also occur along the length of an evolving rift system or passive margin (e.g. McClay et al., 2002; Zwaan et al., 2016; Deptuck and Kendell, 2017; Rowan, 2018), have important effects on subsequent salt tectonic deformation.

While earlier salt tectonic modelling studies have often involved a viscous layer with a constant thickness (e.g. Cobbold et al., 1989; Mauduit et al., 1997; Mauduit and Brun, 1998), more recent modelling efforts have started to explore the effects of initial salt basin geometries on salt tectonics. Fort et al. (2004a, b) pioneered the effects of more realistic salt basins with salt pinching out towards both the upslope and downslope ends of the basin, whereas other researchers have studied the effects base-salt relief at various wavelengths. For instance, Gaullier et al. (1993), Maillard et al. (2003), Adam and Krezsek (2012), Dooley et al. (2017), Dooley et al. (2017, 2018), Ferrer et al. (2017) and Pichel et al. (2018, 2019) describe the influence of single or multiple (oblique) basement steps or sub-salt seamounts and ridges on salt tectonic systems. Depending on whether they represent a thinning or a thickening of the salt layer, such short wave length steps and obstacles within a salt basins can either accelerate or decelerate salt flow through basal drag (Dooley et al., 2017). If sufficiently reducing salt thicknesses, base-salt relief may divide the system in different segments behaving as separate salt basins, with contractional structures upslope and (enhanced) extensional structures downslope of the relief (e.g. Dooley et al., 2017; Ferrer et al., 2017; Jackson and Hudec 2017). The specific arrangement of such base-salt relief can lead to highly complex deformation structures, with important variations both along and across a margin (e.g. Dooley et al. 2017; Dooley et al., 2018).

Yet these modelling studies generally aim to simulate specific (features of) salt basins and the resulting salt tectonic deformation, and although some studies have included various salt basin shapes, these are somewhat limited in their scope since they either aim to mimic specific natural examples (e.g. Adam and Krezsek, 2012) or remain rather conceptual, involving artificial geometries (e.g. Albertz and Beaumont, 2010). We thus conclude that the effect of long wave length salt basin geometry, specifically initial salt depocenter location, on salt tectonics remains to be explored more systematically, providing an incentive for further research. In this paper we therefore build on previous work exploring the effects of basin geometry on salt tectonics by systematically testing the influence of (1) initial salt basin depocenter location and (2) initial mean salt thickness on salt tectonic systems through simple brittle-viscous (and viscous-only) analogue experiments.

## 2. Experimental methods

### 2.1. Model materials

Our analogue models involved a brittle-viscous model configuration, which is routinely used for salt tectonic modelling studies (e.g. Cobbold and Szatmari, 1991; Gaullier et al., 1993; Mauduit and Brun, 1998; Fort et al., 2004a, Brun and Fort, 2011; Gaullier and Vendeville, 2005; Ge et al., 2019a, b). To represent a basal salt layer in a salt tectonic system we applied a locally up to 10 mm thick body of transparent silicone (polydimethylsiloxane or PDMS, type SGM-36 produced by Dow Corning), with a density (ρ) of ca. 965 kg/m$^3$ and viscosity (η) of ca. 3·10$^4$ Pa s Weijermars 1986; Rudolf et al., 2016; Zwaan et al., 2018). This viscous material has a Newtonian rheology (n = ca. 1) under standard experimental conditions, which makes it very suitable for modelling salt flow (e.g. Fort et al., 2004a, b). A 6 mm thick layer of fine-grained (ø = 200–300 μm), homogeneously sorted and well-rounded Fontainebleau quartz sand was used to represent brittle post-salt (suprasalt) sedimentary cover. This sand has an internal friction coefficient (μ) of ca. 0.6 and negligible cohesion (Vendeville et al., 1987; Fort et al., 2004a), making it a suitable analogue for brittle materials in nature (Klinkmüller et al. 2016). The sand is sieved onto the PDMS layer below in order to ensure a constant density of ca. 1400 kg/m$^3$. Note that the resulting density contrast between salt and sediment layers in the models is slightly exaggerated. Material characteristics are summarized in Table 1.

### 2.2. Model set-up

For this study we tested a total of ten salt basin geometries (Fig. 2), which were subdivided in two sets of five salt basin geometries each (Fig. 2). The first set (basin shapes 1–5) consisted of salt basins with a single 10 mm deep depocenter (3 km in nature) that all have the same mean salt basin depth (5 mm) (Fig. 2a). The use of this general single-depocenter geometry for salt tectonic modelling was first introduced by Fort et al. (2004a, b) based on the initial salt distribution in post-rift evaporite basins along the Angolan margin (e.g. the Lower Congo Basin, Fig. 2d) and has been used routinely by other studies since (e.g. Ge et al., 2019a, b). We systematically varied the location of the salt depocenter between the basins (defined by distance D, measured from the upslope

**Table 1**
Material properties.

| | |
|---|---|
| **Granular material: Fontainebleau quartz sand**[a] | |
| Grain size range | 200–300 μm |
| Density (sieved) (ρ) | 1400 kg/m$^3$ |
| Angle of internal friction (φ) | 30–33° |
| Coefficient of internal friction (μ) | 0.58–0.65 |
| Cohesion (C) | negligible |
| **Viscous material: SGM-36 PDMS**[b] | |
| Density (ρ) | 965 kg/m$^3$ |
| Viscosity[c] (η) | ca. 2.8·10$^4$ Pa s |
| Rheology | Newtonian (n ~ 1)[d] |

[a] Quartz sand characteristics after Vendeville et al. (1987) and Fort et al. (2004a).
[b] Pure PDMS rheology after Rudolf et al. (2016).
[c] Viscosity value holds for model strain rates < 10$^{-2}$ s$^{-1}$.
[d] Power-law exponent n (dimensionless) represents sensitivity to strain rate and holds for model strain rates < 10$^{-2}$ s$^{-1}$.

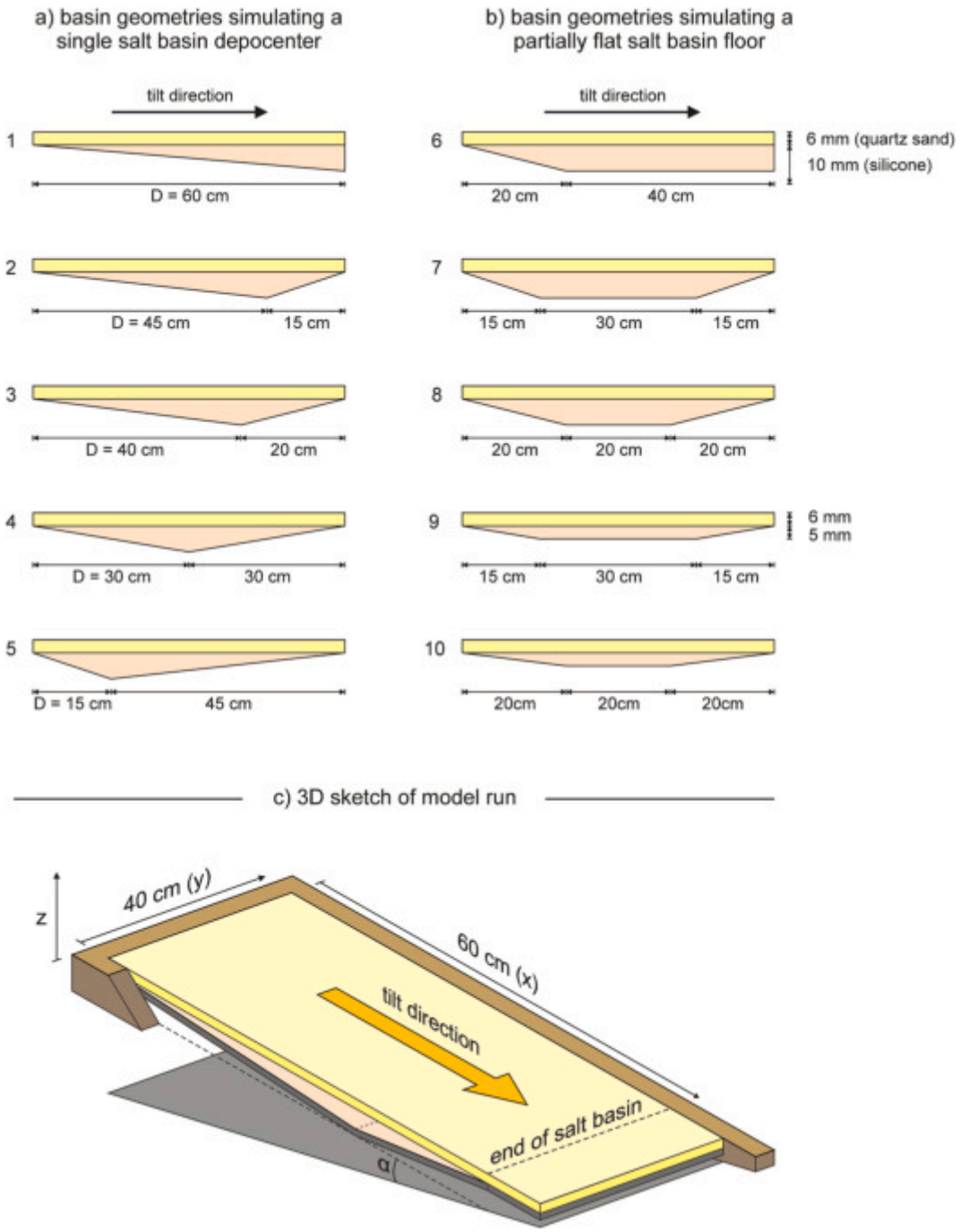


**Fig. 2.** Model set-up. (a) Salt basin geometries 1–5 with a single depocenter, where the maximum model salt thickness is 10 mm. Note that D is defined as the distance between the upslope edge of the model salt basin and the basin depocenter. (b) Basin geometries 6-10 involving a partially flat basin floor, with a maximum model salt layer thickness of 5 mm for basin geometries 9 and 10, instead of the standard 10 mm. (c) 3D Sketch of model run, during which the basin is tilted by either 1° or 3° (angle α) towards the positive x-direction. These sketches represent models from Series I and II (experiments with a brittle cover), but the same salt basin shapes without sand cover were applied for Series III (see the Appendix for results from this model series). Model details are listed in Table 2.

edge of the basin). From model to model, the salt depocenter location was shifted upslope to simulate different basin shape (e.g. the Scotian Margin, Fig. 2f). As a result, also the basin floor inclination and the change in salt thickness as a function of the distance from the model salt depocenter on both sides varied from model to model. The first basin in this set (basin shape 1) represented the extreme endmember of a half-graben structure filled with syn-rift salt, and with the abrupt downslope buttress representing a steep boundary fault (Fig. 2a).

The second set of model salt basin geometries (basins shapes 6–10) involved basin geometries with a central flat part of the basin floor (Fig. 2b). These were used to represent basins with varying mean salt isopachs, either by varying the extent of the flat basin floor and/or reducing the maximum thickness of the salt layer from the regular 10 mm–5 mm (basin shapes 9 and 10, Fig. 2a and b). The gentle basin floor would be typical of post-rift salt basins, but similar to basin shape 1, the steep downslope end of basin shape 6 would imply syn-rift salt deposition in a halfgraben-like structure with a boundary fault at the downslope basin end (Fig. 2b). Alternatively, the steep downdip salt barrier could represent a volcanic high as observed in the Kwanza and Santos Basins, each on opposite sides of the South Atlantic (Quirk et al., 2012).

All model salt basins were 60 cm long (x-axis) and 40 cm wide (y-axis), translating to 180 × 120 km in nature. They were made out of parts of PVC (for the basin floor) and wood (for the vertical upslope and side edges of the models) (Fig. 2c). These parts were fully covered with regular duct tape to seal any slits between them and to ensure homogeneous boundary conditions in all models. The basins were filled with the PDMS silicone oil representing the model salt layer, on top of which the 6 mm thick suprasalt cover of homogeneous Fontainebleau sand was added. This sand cover extended for ca. 10 cm beyond the salt basin's downslope end (Fig. 2). After model preparation, the models were instantaneously tilted by either 1 or 3°, to simulate the marginal inclination due to differential thermal subsidence (Fig. 1a–c). Following this initial tilting, the models were left to evolve for two days (48 h). No syntectonic sedimentation was applied.

We completed a total of 35 experiments, including reruns (Table 2) that are divided in three series. The first series (Series I) contains all experiments simulating a 1° margin tilt (Models A-J). The second series (Series II) contains experiments with a 3° margin tilt (Models K–W, where the Models U–W were reruns of Models P-T, the results of which are provided in the supplementary material, Zwaan et al., 2021). As a reference, we also completed a third series (Series III) involving models without a sand cover in which we aimed to reproduce the response of a purely viscous system. The total lack of a suprasalt sediment cover is likely unrealistic, hence the results of these models are not part of the main text and are shown in the Appendix only.

### 2.3. Analogue model scaling

Analogue models scale down from nature in terms of geometry, kinematics and dynamics (e.g. Hubbert, 1937; Ramberg, 1981). Based on dimensionless numbers representing ratios of forces, scaling factors for the basic dimensions of length, mass and time are derived. Here we used the ratio between lithostatic pressure and viscous strength (the so-called Ramberg number $R_m$)

$$R_m = \rho g h^2 / \eta v \quad (1)$$

where ρ represents density, g the gravitational acceleration, h height, η dynamic viscosity and (v) velocity, to scale the viscous regime (e.g. Ramberg, 1981; Adam and Krezsek, 2012; Gemmer et al., 2005). In the brittle regime, the friction coefficient μ defining the depth dependency of frictional strength, was used as a dimensionless parameter for cohesionless materials. By keeping μ and $R_m$ similar in the model and in nature (ca. 0.6, Table 3) scaling factors for all relevant dimensions and parameters can be derived. From equation (1), it follows that the time scale ratio (t*) depends directly on the initial choice of length scale, density and viscosity for experiments conducted under normal gravity (convention: $\rho^* = \rho_{model}/\rho_{nature}$):

$$t^* = \rho^* g^* h^* / \eta^* \quad (2)$$

In this study, the geometric scaling or height ratio (h*) was $3.3{\cdot}10^{-6}$ (1 cm in the model is 3 km in nature). The time scaling (t*) was subsequently dictated by the effective density (i.e. reduced by the water density for submarine systems by a factor of c. 1/2) and the ratio between the viscosity of natural salt versus silicone oil at typical model strain rates, is in the order of $5{\cdot}10^{-16}$ (Table 3). Therefore, 1 h in the model translated to approximately 0.6 Myr in nature and the standard model duration of 48 h represented 29 Myr of basin evolution. We note that while the friction coefficient of our brittle cover analogue was similar to nature (ca. 0.6), the density ratio between the brittle viscous materials in our models was somewhat higher than in nature (1.45 in our models vs. 1.05 in nature). This resulted in buoyancy forces which were slightly exaggerated but this was not considered to be problematic in our experiments.

Furthermore, the models should have similar proportions as their natural prototype. Salt basins in nature are usually some hundreds of kilometres large (L) and a few kilometres deep (h), giving an L/h ratio of $10^2$-$10^3$ (e.g. Brun and Fort, 2011; Strozyk et al., 2017). The salt basin analogues in this study were 60 cm long (measured across-margin) and the simulated salt layers were 0.5–1 cm deep at the deepest point (translating to 180 km and 1.5–3 km, respectively). These dimensions yielded an L/h ratio ranging from 60 to the order of $10^2$, which we deem sufficiently close to the natural values to state that our models were adequately scaled. An overview of scaling parameters is provided in Table 3.

### 2.4. Analogue model analysis

All models were monitored by means of top view topography; digital images of the models were taken every 15 min (12 min for some) for the duration of the model run using customer grade 10 megapixel cameras. A grid of equidistant dots with laterally reduced spacing (5 cm vs. 2.5 near the long ends and downslope end of the model salt basins), made of black dyed sand, was applied on the model surface which allowed a visual appreciation of surface deformation.

Furthermore, by sieving fine coffee powder on top of the model surface we created a random pixel pattern for digital image correlation (DIC) analysis. Particle Image Velocimetry methods (PIV, e.g. Adam et al., 2005; Boutelier et al., 2019 and references therein) allowed for quantification of 2D horizontal surface displacement monitoring at high precision (<0.1 pixel). We used commercial LaVision Davis 8 software applying 2D-DIC processing through a least squares method with subset and step sizes of 59 and 10 pixels, respectively. With an effective image

**Table 2**
Model details.

| Basin Geometry[a] | Depocenter location (distance D) | Mean silicone (model salt) layer thickness | Series I (6 mm thick brittle cover, 1° basin tilt) | Series II (6 mm thick brittle cover, 3° basin tilt) | Series III (no brittle cover, 3° basin tilt)[c] |
|---|---|---|---|---|---|
| | | | Model name | Model name | Model name |
| 1 | 60 cm | 5.0 mm | A | K | Z1[d] |
| 2 | 45 cm | 5.0 mm | B | L | Z2[d] |
| 3 | 40 cm | 5.0 mm | C | M | Z3[d] |
| 4 | 30 cm | 5.0 mm | D | N | Z4[d] |
| 5 | 15 cm | 5.0 mm | E | O | Z5[d] |
| 6 | – | 8.3 mm | F | U (P[b]) | Z6 |
| 7 | – | 7.5 mm | G | V (Q[b]) | Z7 |
| 8 | – | 6.7 mm | H | W (R[b]) | Z8 |
| 9 | – | 3.8 mm | I | X (S[b]) | Z9 |
| 10 | – | 3.3 mm | J | Y (T[b]) | Z10 |

[a] See Fig. 2 for basin geometry description.
[b] Test runs of models U–Y without stereographic photos, not discussed in this paper. For results see the supplementary materials (Zwaan et al., 2021).
[c] Series III models are presented in Appendix A1 only.
[d] Model ran for 49 h instead of 48 h.

**Table 3**
Scaling parameters.

| | General parameters | | Brittle sediments | | Ductile evaporites | | Dynamic scaling | |
|---|---|---|---|---|---|---|---|---|
| | Gravitational acceleration $g$ (m/s$^2$) | Height $h$ (m) | Density $\rho$ (kg/m$^3$) | Friction coefficient $\mu$ | Density $\rho$ (kg/m$^3$) | Viscosity $\eta$ (Pa s)[a] | Velocity $v$ (m/s) | Ramberg number $R_m$ |
| Model | 9.81 | 0.01 | 1400 | 0.6 | 965 | $2.8{\cdot}10^{4}$ | $5.8{\cdot}10^{-7}$ | 58 |
| Nature | 9.81 | 3000 | 2300 | 0.6 | 2200 | $5{\cdot}10^{19}$ | $7.9{\cdot}10^{-11}$ | 49 |
| Ratio | 1 | $3.3{\cdot}10^{-6}$ | 0.61 | 1 | 0.44 | $5.6{\cdot}10^{-16}$ | $7.3{\cdot}10^{4}$ | 1.2 |

[a] Natural salt viscosities may vary significantly (between $10^{14}$ and $10^{20}$ Pa s, Jackson and Talbot, 1986, and references therein).

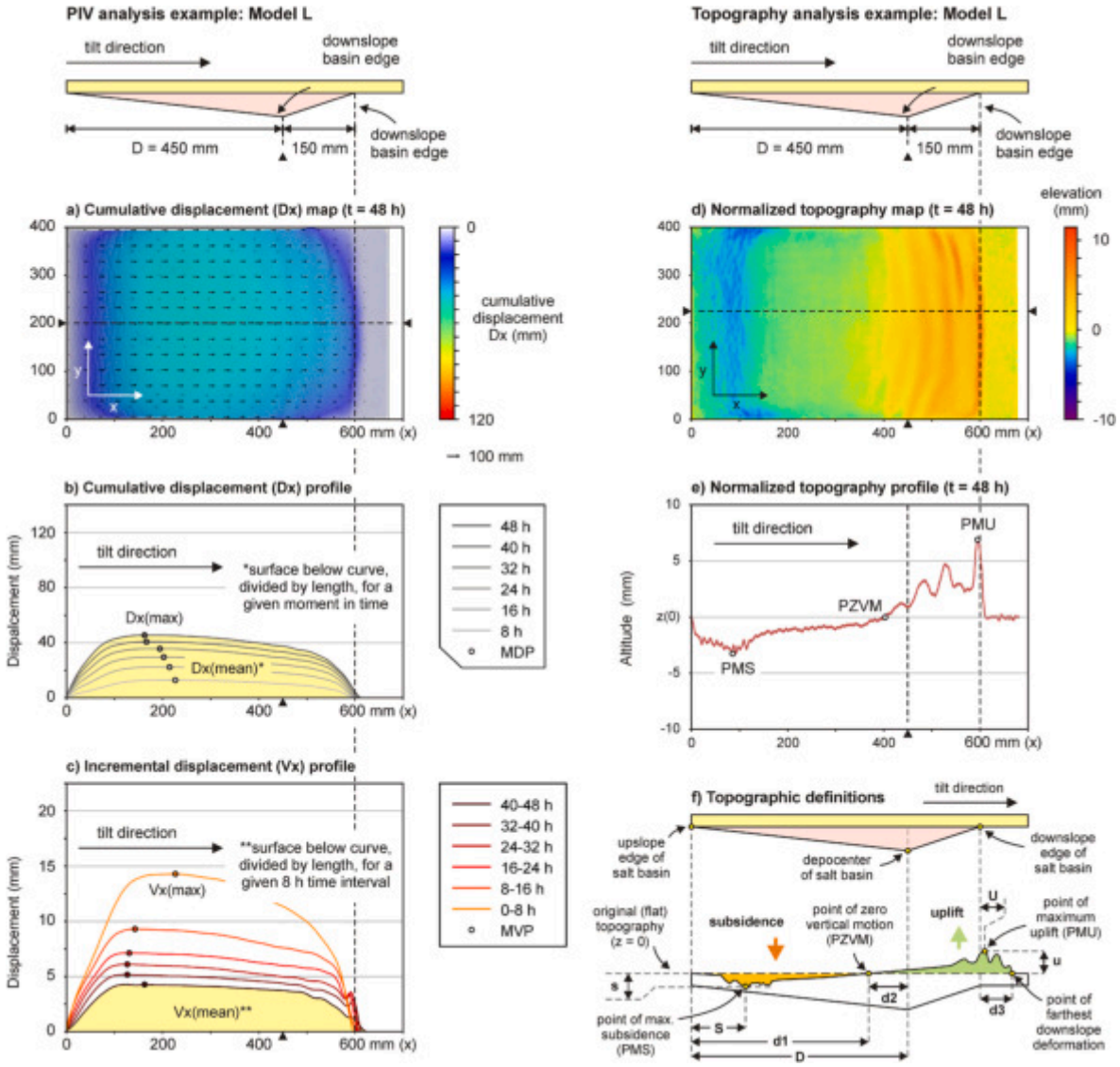


**Fig. 3.** Definitions used for PIV analysis and topography analysis (example: Model L with depocenter location at distance D = 450 mm from the upslope salt basin end). (a) Final cumulative surface displacement (Dx) presented in map view (t = 48 h). (b) Cumulative downslope displacement (Dx) evolution plotted along a central profile indicated in (a). MDP: maximum displacement point, where Dx is highest at specific moment in time: Dx (max). Dx (mean) is the mean cumulative displacement over a specific time interval, calculated by dividing the surface below the Dy curve by its length (c) Incremental downslope displacement (i.e. displacement velocity, Vx). evolution along a central profile indicated in (a). MVP: maximum velocity point, where Vx is highest for a specific time interval: Vx (max). Vx (mean) is the mean displacement over a specific time interval, calculated by dividing the surface below the Vy curve by its length. (d) Normalized final topography presented in map view. (e) Normalized final topography presented along a profile indicated in (d). PMS: point of maximum subsidence, PMU: point of maximum uplift, and PZVM: point of (final) zero vertical motion, i.e. the intersection of the final model topography profile with z = 0. (f) Topographic parameters. D: distance between depocenter and upslope salt basin end, d1: distance between upslope end of basin and PZVM, d2: distance between depocenter and PZVM, d3: distance between downslope end of basin and point of farthest downslope deformation, S and s: location and amount of maximum vertical subsidence in the upslope extensional domain, U and u: location and amount maximum uplift in the downslope contractional domain. The colored surfaces below and above the topography curve (orange and green, respectively) are of equal size, each indicating the displaced mass along the profile. (For interpretation of the references to color in this figure legend, the reader is referred to the Web version of this article.)

resolution of ca. 0.5 mm per pixel, incremental displacements were derived with a precision of ca. 50 μm. The resolution of the displacement field (grid point spacing) defined by the step size is about 5 mm.

PIV analysis yields incremental downslope displacement (or velocity, Vx) and cumulative downslope displacement (Dx) data accumulated over the duration of a model run. These data are documented in maps of finite surface displacement showing total displacement accumulated over a model run, as well as in profiles extracted along the central axis of each model over 6 intervals of 8 h each (Fig. 3). These profiles illustrate the evolution of surface displacement, where Dx-plots provide the model development in terms of cumulative surface displacement, while Vx-plots visualize incremental displacement (velocity) variations over time. Note that in principle, Dx is the sum of Vx. The plots also provide the location and amount of maximum incremental and cumulative displacements for each time interval (i.e. $Vx_{max}$ measured at the maximum velocity point [MVP] and $Dx_{max}$ at the maximum (cumulative) displacement point [MDP], respectively), Fig. 3). Besides the $Vx_{max}$ and $Dx_{max}$ values that represent strictly point values, we also derived the mean cumulative and incremental displacements over time (i.e. $Dx_{mean}$ and $Vx_{mean}$, respectively) by taking the area below the relevant curve, divided by the curve's length,which we took as a proxy for model-wide deformation (Fig. 3b and c).

In addition, we also took photographs of our experiments from different perspectives at the start and end of each model run. These images allow reconstruction of the model surface with the use of photogrammetry software (Agisoft Photoscan), based on the Structure-from-Motion method (SfM, Westoby et al., 2012), and was used here to analyze the vertical component of model deformation not captured by 2D PIV analysis. The digital elevation models (DEM) of the start and end of each model run served to create normalized topography maps with an error below ± 0.5 mm. We also extracted normalized final topographic profiles along about the same central axis of the model we used for the PIV profiles, complementing the horizontal displacement results derived by PIV analysis (Fig. 3).

We subsequently analyzed a total of eight individual morphometric parameters on the normalized final topographic profiles, of which the definitions are as follows. Total mass displacement is the area of the subsided part of the profile that equals the uplifted part of the profile (shown in orange and green in Fig. 3f, respectively). The maximum subsidence (s) is measured at the point of maximum subsidence (PMS), i.e. the deepest part of the depression in the upslope extensional domain. The location of the PMS is defined by distance S, measured from the upslope salt basin end. Vice versa, the maximum uplift (u) is measured at the point of maximum uplift (PMU), i.e. the highest point in the downslope compressional domain, the location of which is defined as distance U. Distance d1 is the distance between the point of (final) zero vertical motion (PZVM, i.e. where the profile cuts the altitude [z] = 0 line) and the salt basin upslope end, whereas distance d2 is the distance between the PZVM and the basin depocenter. Distance d3 is the distance between the farthest downslope limit of deformation and the downslope edge of the salt basin.

## 3. Results

### 3.1. Qualitative observations from plan view visual inspection

We present a snapshot of final model surface structures in Fig. 4, highlighting some of the general characteristics of our experiments. Models with 1° basin tilt (Models A and F from series I, Fig. 4a and b) generally showed, apart from a slight downslope displacement of the surface grid, almost no visible deformation in the sand layer. Only some minor folding occurred at the downslope basin edge in Model F (which had the highest mean salt thickness of all Series I models, see Table 1) accompanied by slight extensional faulting at the upslope basin end.

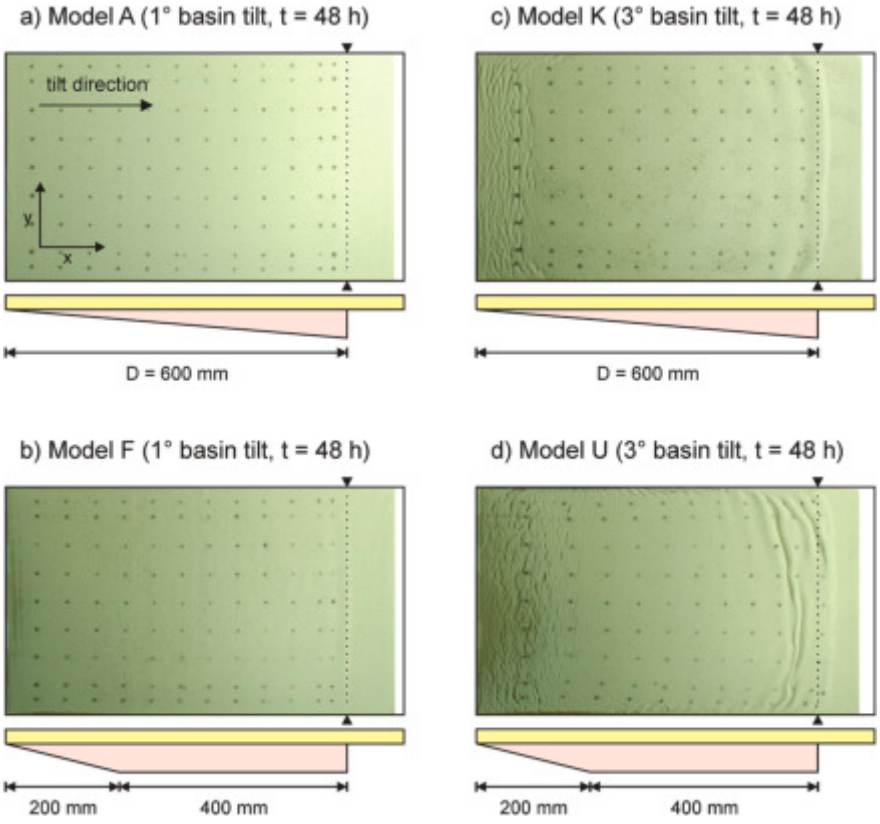


**Fig. 4.** Overview of final surface structures (t = 48 h) of selected experiments with basin geometries 1 and 6 illustrating general model behavior. (a–b) Models A and F from series I, tilted by 1°. (c–d) Models K and U from series II, tilted by 3°. Note that the initial distances between the surface markers was not constant (see description in Section 2.4): the markers in (a) and (b) are almost in situ.

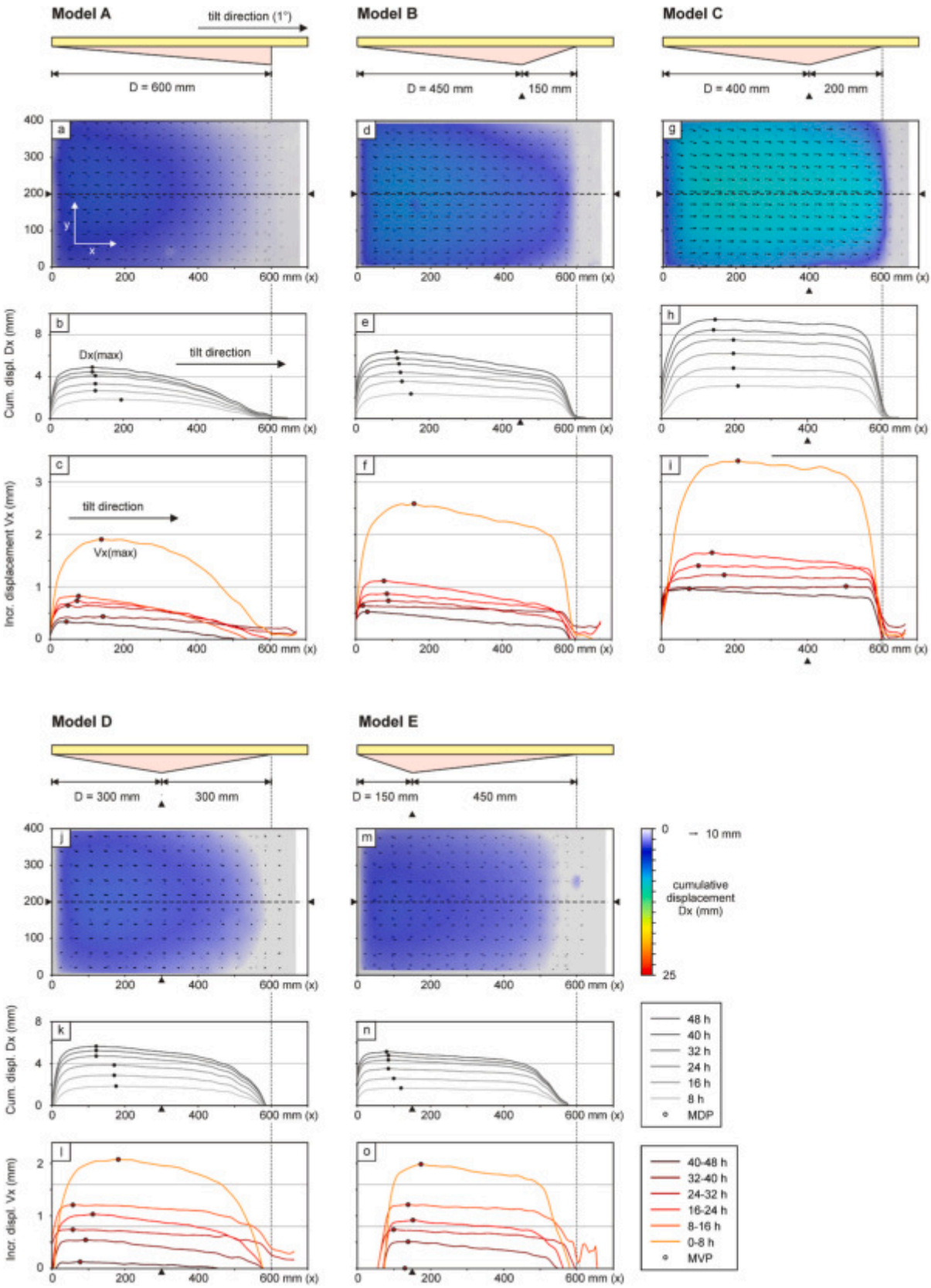


**Fig. 5.** PIV-derived surface displacements of models A-E from series I (1° basin tilt, basin shapes 1–5, with constant mean model salt thickness), shown in both map view (Dx only) and plotted on along-axis profiles (both Dx and Vx). MDP: maximum displacement point. MVP: maximum velocity point. For more details on definitions, see Fig. 3.

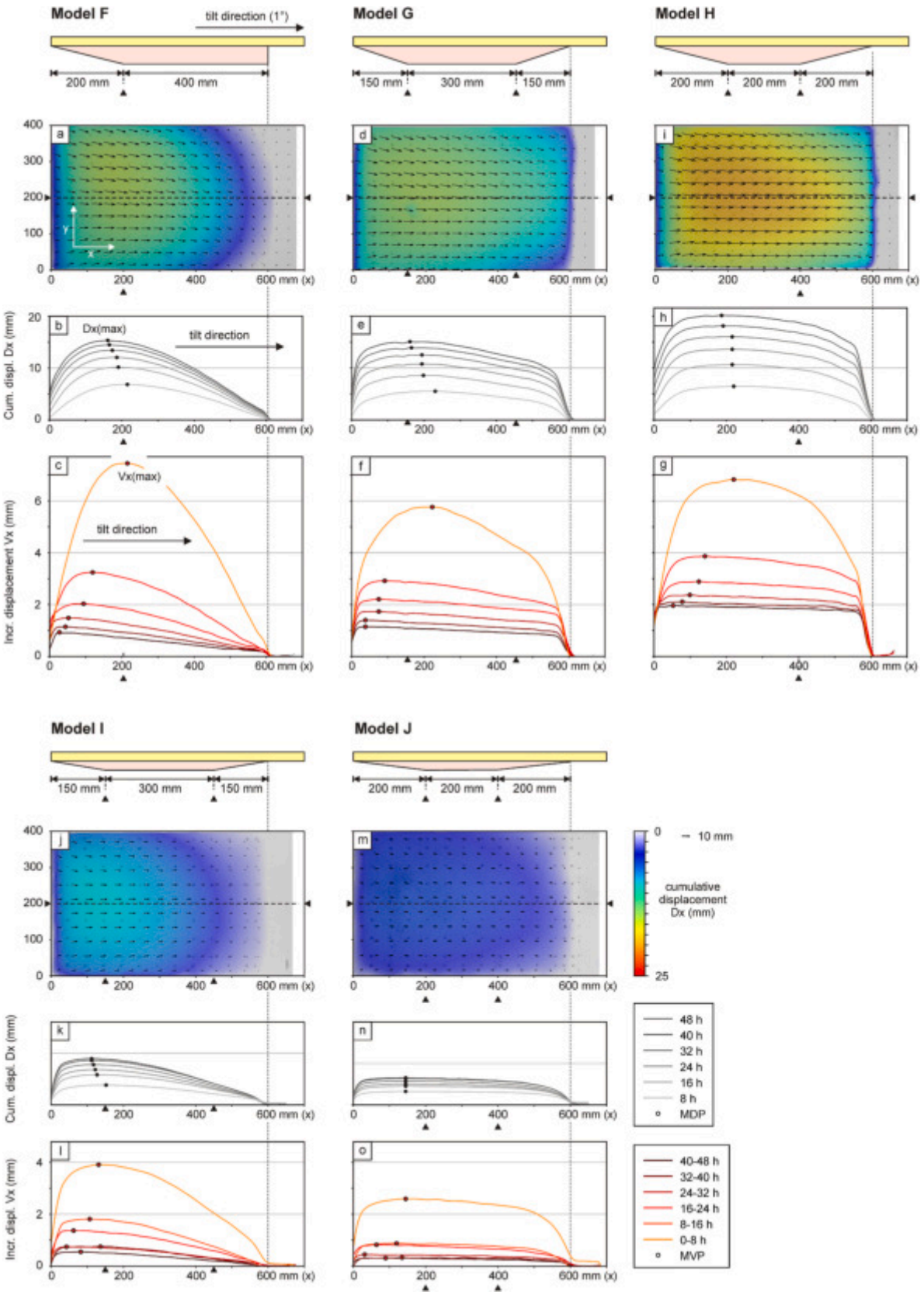


**Fig. 6.** PIV-derived surface displacements of models F-J from series I (1° basin tilt, basin shapes 6–10, with constant mean model salt thickness), shown in both map view (Dx only) and plotted on along-axis profiles (both Dx and Vx). MDP: maximum displacement point. MVP: maximum velocity point. For more details on definitions, see Fig. 3.

By contrast, experiments with 3° basin tilt (Models K and U from series II, Fig. 4c and d) developed clear extensional structures in their upslope domain, as well as contractional structures at the downslope margin of the model salt basin with a zone of translational displacement in between. The contractional structures even migrated beyond the downslope end of the model salt basin, forming a salt-cored overthrust. These structures are more pronounced in Model U, which has the highest mean salt thickness of all Series II models. In these 3° basin tilt experiments we also observed a curving of structures along the long edges of the model (concave downslope orientations for extensional features and convex upslope curving folds and thrusts in the compressional domain) reflecting the effect of lateral drag due to boundary friction there (e.g. Fort et al., 2004b; Ge et al., 2019a).

### 3.2. Quantitative results from series I (1° basin tilt models)

From visual inspection on top view imagery (section 3.1), we identified that the degree of margin tilt is an important factor in our models: the models with 1° basin tilt from Series I exhibit very limited deformation. Accordingly, the DEM analysis generally did not show a significant enough topographic signal in most models. By contrast, PIV analysis was sensitive enough to provide some useful insights into the evolution and deformation of the 1° basin tilt models and its results are reported below (Figs. 5 and 6).

Models A-E from Series I all (with constant mean model salt thickness) showed very similar displacement patterns (Fig. 5). Deformation was registered above the whole extent of the model salt basins and the displacement curves (both the Dx and Vx curves) generally formed a plateau between an upslope increase in displacement and a downslope decrease in displacement. These sections of the curves represent an upslope extensional domain, and a downslope compressional domain with a translation-dominated domain in between. The plateau itself was often slightly tilted towards the downslope end of the model, indicating a very minor (<1%) distributed shortening within the translation domain. Only Model A deviated from this pattern, as it developed bell-shaped displacement curves with the top towards the upslope end of the profiles indicating a general downslope decrease in displacement representing more distributed shortening (Fig. 5a–c). We found that maximum final displacements ($Dx_{max}$) generally ranged between 5 and 7 mm, with a maximum for Model C, in which $Dx_{max}$ was ca. 8 mm. Importantly, the Vx plots show that a major part of this displacement occurred in the earliest phases of the model runs, after which downslope displacement rates quickly decreased before stabilizing towards the end of the experimental run (Fig. 5c, f, i, l, o). Notably, the translation domain was established very early during the evolution in most models (i.e. during the first 8 h increment) as manifested by a plateau in the first member of the array of Vx curves. However, Vx values in the translation domain of each model slowly decreased towards the downslope end of the model, as also indicated by the upslope location of the MVP.

PIV analysis of Models F-J from Series I (with varying mean model salt volumes and different maximum salt basin depths) revealed displacement patterns with very similar styles to those observed in Models A-E, i.e. plateau and bell-shaped displacement curves (Figs. 5 and 6). Models F–H, with thicker mean model salt thicknesses) showed significantly higher overall displacements compared to Models A-E (final $Dx_{max}$ value between 15 and 20 mm versus 5–8 mm, Figs. 5, 6a-g). By contrast, the total displacement values in the shallow model salt basins of Models I and J remained relatively low (final $Dx_{max}$ values of ca. 3.5 and 2, respectively). While similar to Models A-E in that displacement generally decelerated over the model runs, the translational domain in Models F-J seems to have been established slightly later, i.e. during the second increment of deformation (8–16 h), as indicated by the more bell-shaped first member of the array of Vx curves (Fig. 5). Also in these models, the Vx values in the translational domain gently decreased towards the downslope end of the model, and the MVP was situated upslope.

### 3.3. Quantitative results from series II (3° basin tilt models)

For this model second model series both topography (SfM) and surface displacement (PIV) analysis yielded good results. We start each of the following sections accordingly with the results from topography analysis and then show the results for displacement analysis.

#### 3.3.1. Models K–O (with constant mean model salt thickness)

Based on visual inspection of map view imagery in section 3.1 we showed that Models K and U with 3° basin tilt developed distinct deformation features in the shape of extensional structures in the upslope parts, and contractional structures downslope (Fig. 4c and d). These general features are also clearly visible in the topography analysis results (map view and section view) from models K-O (Fig. 7), and we found some systematic topographic variations associated with the differences in the location of the model salt basin depocenter in these experiment.

In section view we observed a general increase in total mass displacement when the model salt basin depocenter was situated higher upslope (form ca. 430 $mm^2$ to 690 $mm^2$ in section, Fig. 7). This trend also correlates with an increase in maximum subsidence in the extensional domain at the upslope end of the models when the model salt depocenter was positioned higher upslope (from ca. 2.9 mm to 5.5 mm), whereas the maximum uplift recorded in the downslope part was simultaneously decreased (from ca. 8.4 to 6.5 mm) (Fig. 7). Yet within Models K–O, the loci of maximum vertical displacement remained rather stable with changing depocenter locations (Fig. 7). Furthermore, we found that the point of zero vertical motion (PZVM) was found higher upslope in models with a higher upslope model salt depocenter (Fig. 7). Here it is worth noting that the PZVM was situated upslope from the model salt depocenter in Models K-M (Fig. 7a–c), but in Models N and O, the PZVM was higher upslope than the model salt basin depocenter (Fig. 7d–e) so that the PZVM "overtook" the upward model salt depocenter shift from Model K to Model O. Finally, models with a downslope depocenter allowed material to move farther downslope, out of the basin (e.g. Model K, Fig. 7a).

Using the topographic parameters allows a detailed quantification of deformation in these models, yet these parameters do not fully capture specific aspects. For instance, the surface of the translational domain in Models K–O, was clearly tilted due to upslope subsidence and downslope uplift (Fig. 7). In some cases the translational domain also showed the development of a "slope break" as the downslope part of the translational domain was titled to a higher degree with respect to the upslope part (Models L-N, Fig. 7b–d). It should also be noted that the topographic parameters in Model C (basin shape 3) were systematically slightly more pronounced than in the other models (Fig. 7c).

In general, 3° basin tilt models accumulated higher displacements compared to the 1° basin tilt models. While the 1° tilt models with constant mean model salt thickness (Models A-E from Series I) registered final cumulative downslope displacements ($Dx_{max}$) of 5–8 mm (section 3.2, Fig. 4), the equivalent 3° basin tilt Models K–O from series II accumulated up to ca. 50 mm downslope displacement (Fig. 8). Another contrast with the 1° basin tilt models is that the final cumulative displacement ($Dx_{max}$) profiles of Models K–O are distinctly plateau-shaped, indicating the occurrence of three salt tectonic domains (upslope extension, mid-slope translation and downslope contraction). Only a hint of the bell-shaped displacement curves observed in Models A-E can be seen in the initial phases as recorded by the Vx plots (Fig. 8c, f, g, l and o), hinting that the development of the salt tectonic domains was not instantaneous.

Similar to the topographic analysis, detailed PIV analysis of Models K–O reveals clear correlations between model salt basin depocenter location and displacements. We found that models with a more downslope depocenter produced less displacement than those with a more upslope depocenter: Model K registered a $Dx_{max}$-value of 45 mm, whereas Model O registered a $Dx_{max}$-value of ca. 55 mm (Fig. 8i). An

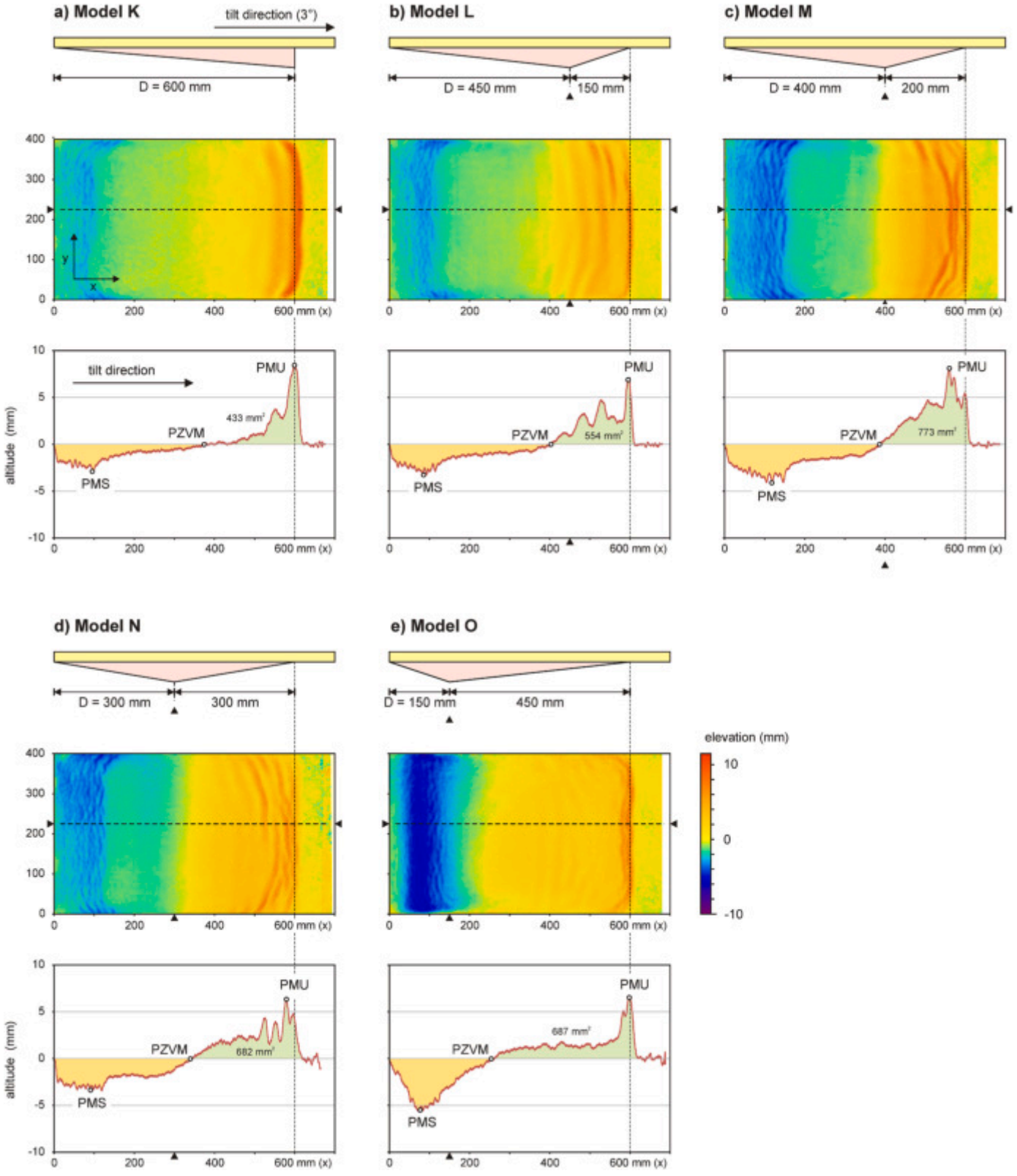


**Fig. 7.** Final normalized topography of Models K–O from Series II (3° basin tilt, basin shapes 1–5 with constant mean model salt thickness) in map view and along a central section. PZVM: point of zero vertical motion, PMS: point of maximum subsidence, PMU: point of maximum uplift. For more details on definitions, see Fig. 3.

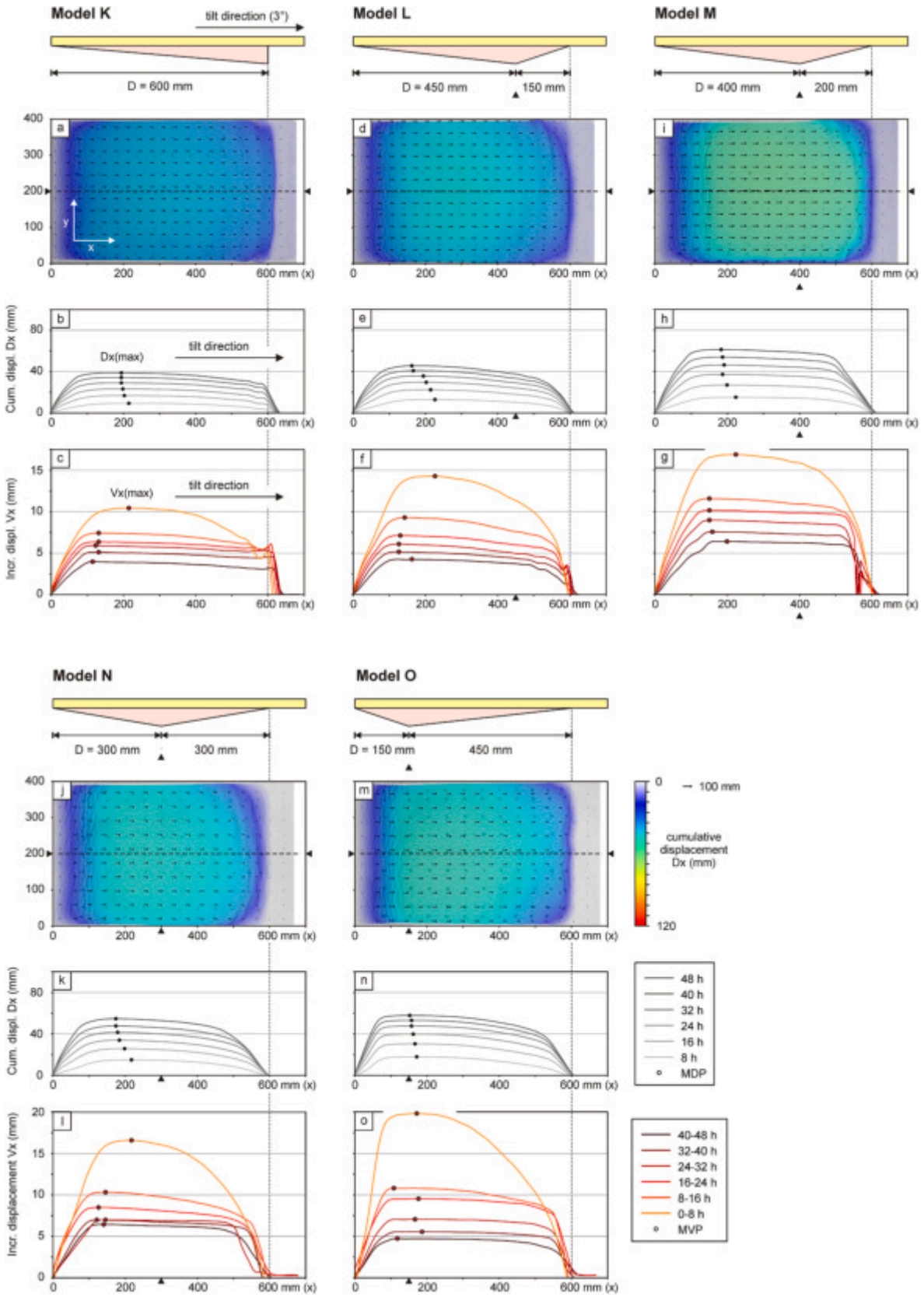


**Fig. 8.** PIV-derived surface displacements of models K–O from series II (3° basin tilt, basin shapes 1–5, with constant mean salt thickness), shown in both map view (Dx only) and plotted on along-axis profiles (both Dx and Vx). MDP: maximum displacement point. MVP: maximum velocity point. For more details on definitions, see Fig. 3.

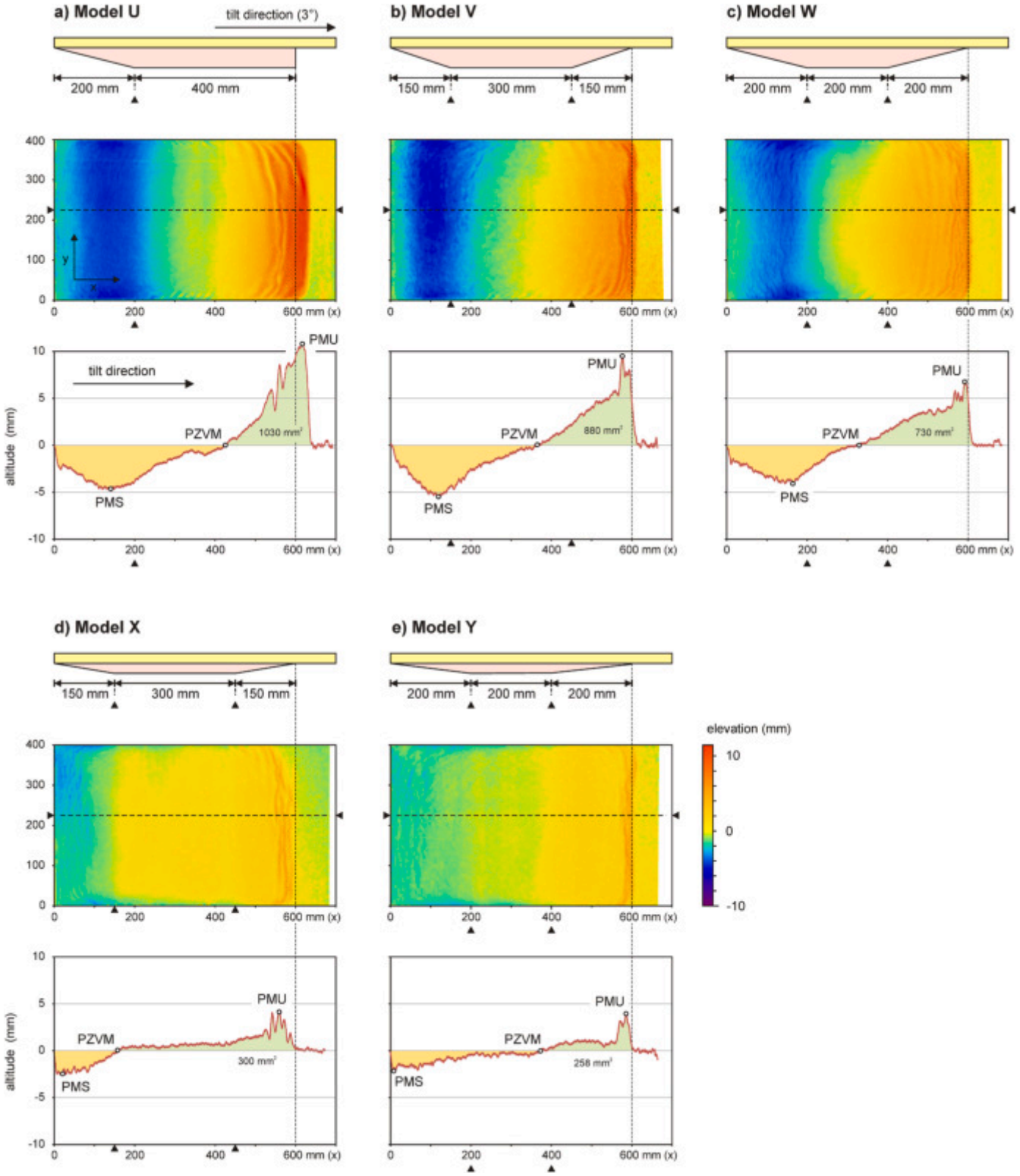


**Fig. 9.** Final normalized topography of Models U–Y from Series II (3° basin tilt, basin shapes 6–10 with varying mean model salt thickness) in map view and along a central section. PZVM: point of zero vertical motion, PMS: point of maximum subsidence, PMU: point of maximum uplift.

exception in this trend was Model M with a $Dx_{max}$-value of 70 mm (Fig. 8i–g) and it may be noted that this particular model salt basin geometry also registered anomalously high displacements in Model C with 1° basin tilt (Fig. 5g–i). All of Models K–O showed an upslope migration of the MDP over time (Fig. 8b, e, h, k, n).

As observed in the models from Series I downslope displacement was highest during the early model stages before it gradually waned towards the end of the model run (Fig. 8c, f, g, l, o). Similar to the $Dx_{max}$ values, the $V_{max}$ values also increased when the model salt basin depocenter was situated higher upslope (from ca. 11 mm in Model K to ca. 20 mm in Model O, Fig. 8c and o, respectively). Furthermore, with the exception of Model O, the MVP systematically showed an upslope migration during early model evolution, often followed by a reverse, downslope path during later stages (Fig. 8c, f, g, l, o).

#### 3.3.2. Models U–Y (with varying mean model salt thickness)

As illustrated in sections 3.1 and 3.2, a higher mean model salt thickness caused increased deformation in our models. This effect was well captured by the final topography of models U–Y from Series II (Fig. 9). Map and profile views of the final normalized topography of these models with 3° basin tilt and varying mean model salt thickness show that Model U (with the highest mean model salt thickness) developed the most pronounced relief (with uplifts up to ca. 12 mm, Fig. 9a). Subsequent Models V and W with gradually decreasing mean model salt thickness also developed gradually less relief (uplifts of ca. 9 mm and 7 mm, respectively, Fig. 9b and c). Furthermore, the very low mean model salt thickness in Models X and Y resulted in very limited relief (Fig. 9d and e). This trend is also captured by the total mass displacement analysis, which consistently drops with decreasing model salt thickness, and ranges from ca. 1000 $mm^2$ in model U to ca. 250 $mm^2$ in Model Y (Fig. 9).

Due to the dominance of the mean model salt thickness in Models U–Y, we did not systematically analyze the various topographic parameters. Yet we identified some potential indications of basin shape influence on final topography. In Models U–W we observed an upslope shift of the PVMZ as the downslope basin floor inclination decreases, analogue to the effect of the model salt basin depocenter location seen in Models K–O (Fig. 7).

PIV analysis of Models U–Y (Fig. 10) revealed similar trends to those observed in their 1° basin tilt equivalents Models F-J (Fig. 6): higher mean model salt thicknesses cause increased displacement. Similar to the total mass displacement analysis from the topography analysis (Fig. 9), the Dx and Vx-values from Models U–Y show a very clear correlation (decreasing from ca. 90 to 35 mm and from ca. 28 to 10 mm, respectively, Fig. 10). A contrast between Models U–Y and Models K–O is that the MDP and MVP remain rather stable in the former (Fig. 10). Yet the initial displacement curves (Vx) did show similar bell-shapes to those in models K–O, which later on developed into plateau-shaped curves with a slight decrease in displacement values towards the downslope end of the model salt basins (Figs. 8 and 10).

### 3.4. Synthesis of key model results

#### 3.4.1. Topography (models K–O and U–Y)

In Fig. 11 we provide a systematic overview of the cross-correlation of key parameters from the topographic analysis with the geometric parameters of our models. We found a very clear correlation between mean model salt thickness and mass displacement (Fig. 11a). Note that due to the very limited topographic development in the 1° models from Series I (see section 3.2), the results from these Series I models are not included in this overview, but this on itself also highlights the strong effect of basin tilt on model salt tectonic deformation. When isolating the models with a constant mean salt thickness and a 3° basin tilt (Models K–O), we could extract the effects of basin shape (i.e. model salt basin depocenter location) on salt tectonic deformation.

Within this context, a more downslope model salt basin depocenter caused a decrease in mass displacement (Fig. 11b). This was associated with an increase in maximum uplift, as well as a decrease in maximum subsidence (Fig. 11c). Yet the locations of maximum uplift and subsidence remained fairly constant (Fig. 11d). We also found that the PZVM was situated higher upslope when the model salt depocenter was located higher upslope, but the PZVM "overtook" the upward shift of the depocenter from Model K to Model O, so the PZVM became situated higher upslope than the model salt basin depocenter in the latter model (Fig. 11e). We also observed that a downslope model salt depocenter more readily allowed material to move out of the basin (Fig. 11f).

#### 3.4.2. Surface displacement (series I and II)

Similar to the results from the topography analysis, the PIV-derived maximum and mean cumulative displacement data ($Dx_{max}$ and $Dx_{mean}$) from Series I and II clearly show the dominant influence of firstly basin tilt and secondly mean model salt thickness on the degree of deformation in our models (Fig. 12a and b). It may be noted that these trends are very similar when considering both measures, showing that $Dx_{max}$ is a good proxy for $Dx_{mean}$ in these models.

When only considering Models K–O with constant mean model salt thickness and 3° basin tilt to filter out the effects of basin tilt and model salt thickness, we found that final cumulative displacement is higher when the model salt basin depocenter is situated higher upslope (Fig. 12c), a result that is very similar to the link between model salt depocenter location and mass displacement from topographic analysis (Fig. 11b). The same trend emerged from the Vx data, although the correlation between depocenter became less strong towards the end of the model runs, as general displacement rates dwindled (Fig. 12d). In general the decay of the maximum displacement rate over time for both Series I and Series II models is quasi exponential, not reaching a steady state rate at the end of the experimental run (Fig. 12e). Furthermore, the location of the MDP in Models K–O was correlated to the model salt basin depocenter as the MDP was found higher upslope when the depocenter was situated higher upslope (Fig. 12f). A somewhat similar trend was also found in Models U–W with changing mean salt thickness (Section 3.3.2, Fig. 9a–c).

Finally, the evolution of the MVP in Models K-O is summarized in Fig. 12g, firstly showing that the initial displacement rates were higher for models with the model salt basin depocenter higher upslope. Subsequently, the graphs shows how displacement rates decreased over time, while the MVP generally migrated upslope. However, this upslope migration of the MVP was in some cases was reversed in the later stages of the model run (Fig. 12g).

## 4. Discussion

### 4.1. Effects of margin tilt and mean salt thickness

Our model results illustrate a strong correlation between the amount of accumulated horizontal displacement or total mass displacement and the tilt angle of the basin: a higher degree of tilting induced more deformation, whereas little deformation was observed with a low degree of tilt (Figs. 11a and 12a and b). This was clearly caused by the forces acting on the models in combination with rheology, in particular that of the model salt, becoming less stable due to larger gravitational forces acting along steeper slopes and thus being more likely to start moving

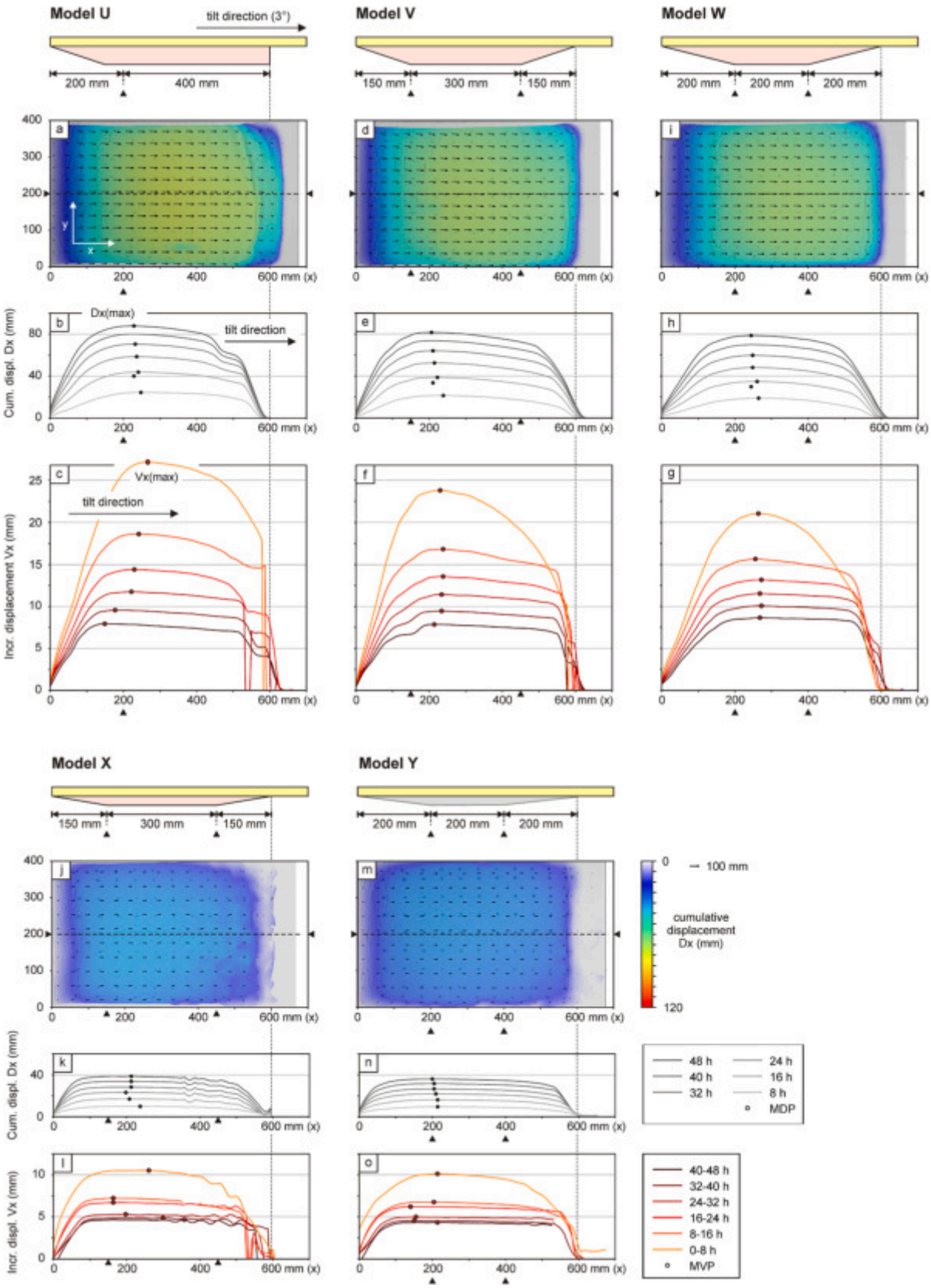


**Fig. 10.** PIV-derived surface displacements of models U–Y from series II (3° basin tilt, basin shapes 6–10 with varying mean model salt thickness), shown in both map view (Dx only) and plotted on along-axis profiles (both Dx and Vx). MDP: maximum displacement point. MVP: maximum velocity point. For more details on definitions, see Fig. 3.

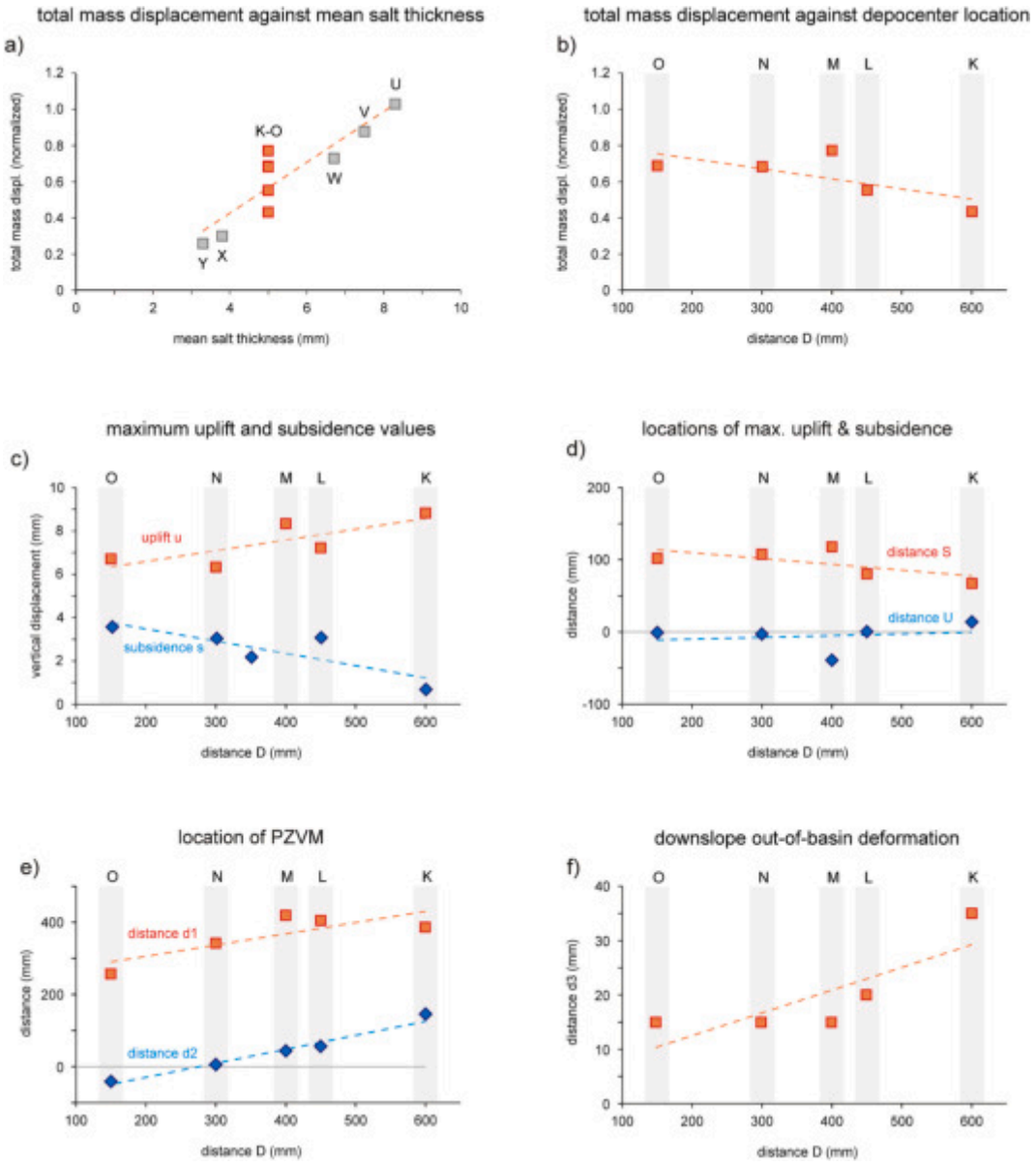


**Fig. 11.** Overview of topography analysis results from Series II experiments with 3° basin tilt (see Fig. 3f for definitions of the various topographic parameters). (a) Total mass displacement against mean model salt thickness in all Series II models. (b–f) Detailed analysis of Models K–O with constant mean layer thickness but different model salt basin depocenter locations, where the model salt basin depocenter location is defined by distance D. (b) Total mass displacement against model salt basin depocenter location (distance D). (c) Maximum uplift (u) and subsidence (s) against model salt basin depocenter location. (d) Location of maximum uplift (U) and subsidence (S) against model salt basin depocenter location (e) Location of the point of zero vertical motion (PZVM), measured from the upslope basin end (d1) and measured from the model salt basin depocenter location (d2), against model salt depocenter location. (f) Maximum downslope propagation of deformation (d3) from the downslope basin end against model salt basin depocenter location. The capital letters in the plots indicate which models the data are derived from.

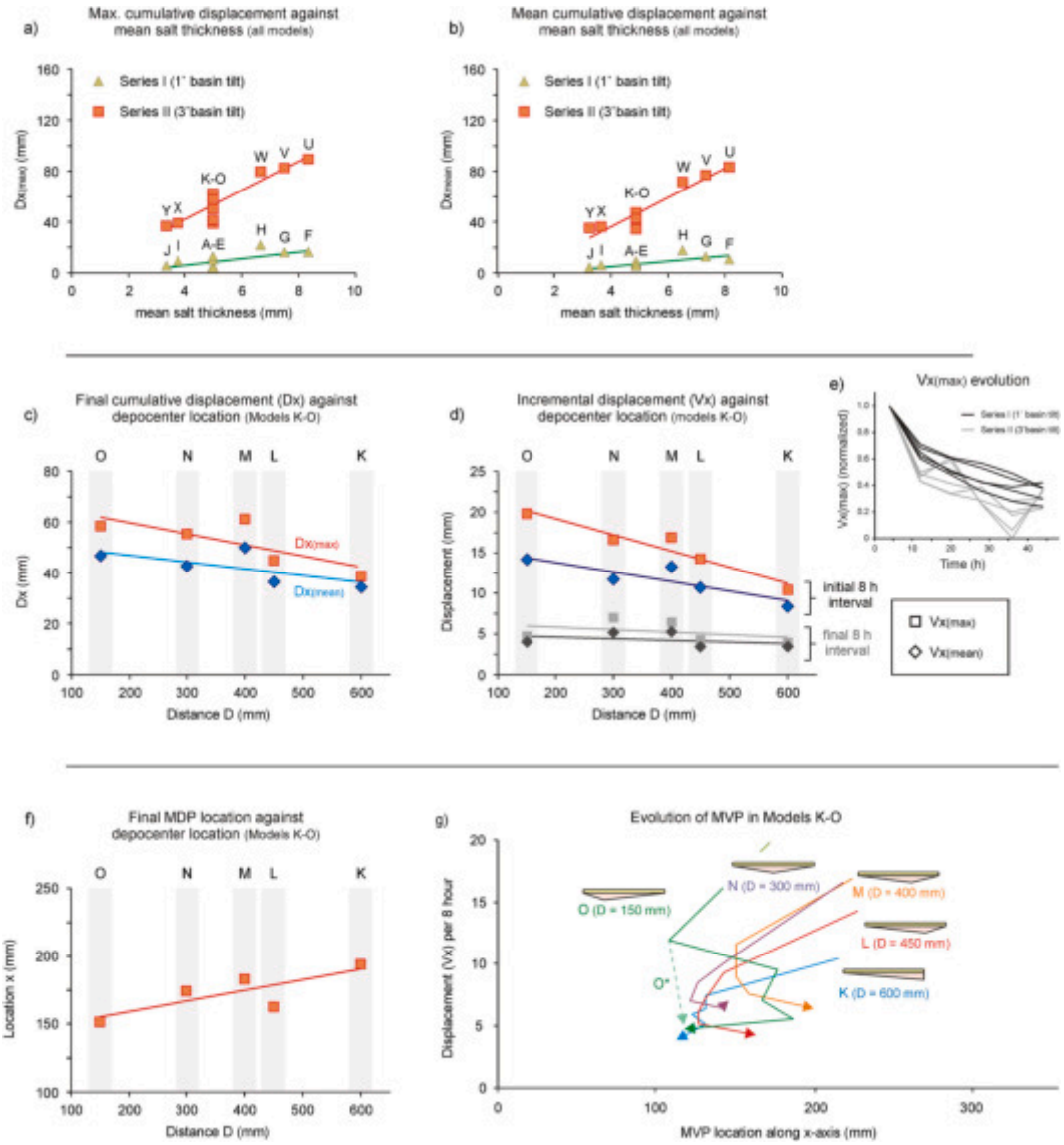


**Fig. 12.** Overview of PIV-derived surface displacement analysis on experiments from Series I and II (For details on the various definitions, see Fig. 3.) (a–b) Relations between and PDMS volume and maximum cumulative displacement ($Dx_{max}$) and total cumulative displacement ($Dx_{mean}$), (c–g) Overview of surface displacement results from Models K–O from Series II (3° basin tilt, constant mean model salt thickness) as a function of model salt basin depocenter location (defined by distance D, see Fig. 3f). (c) Final maximum and mean cumulative displacement values ($Dx_{max}$ and $Dx_{mean}$) against model salt basin depocenter location. (d) Evolution of maximum and mean incremental displacement values ($Vx_{max}$ and $Vx_{mean}$) against model salt basin depocenter location. (e) Comparison (normalized) of maximum incremental displacement ($Vx_{max}$) evolution in Models A-E and K–O. (f) Relation between the location of the maximum displacement point (MDP) and basin depocenter location. (g) Evolution of the maximum velocity point or MVP (location and associated $Vy_{max}$) over time for Models K–O. The arrows indicate the direction of evolution. O*: Note that the continuous line for Model O shows the real data that may contain a slight error, where the dotted line indicates a path that would be more in line with the other experiments. The capital letters in the plots indicate which models the data are derived from. For more details on definitions, see Fig. 3.

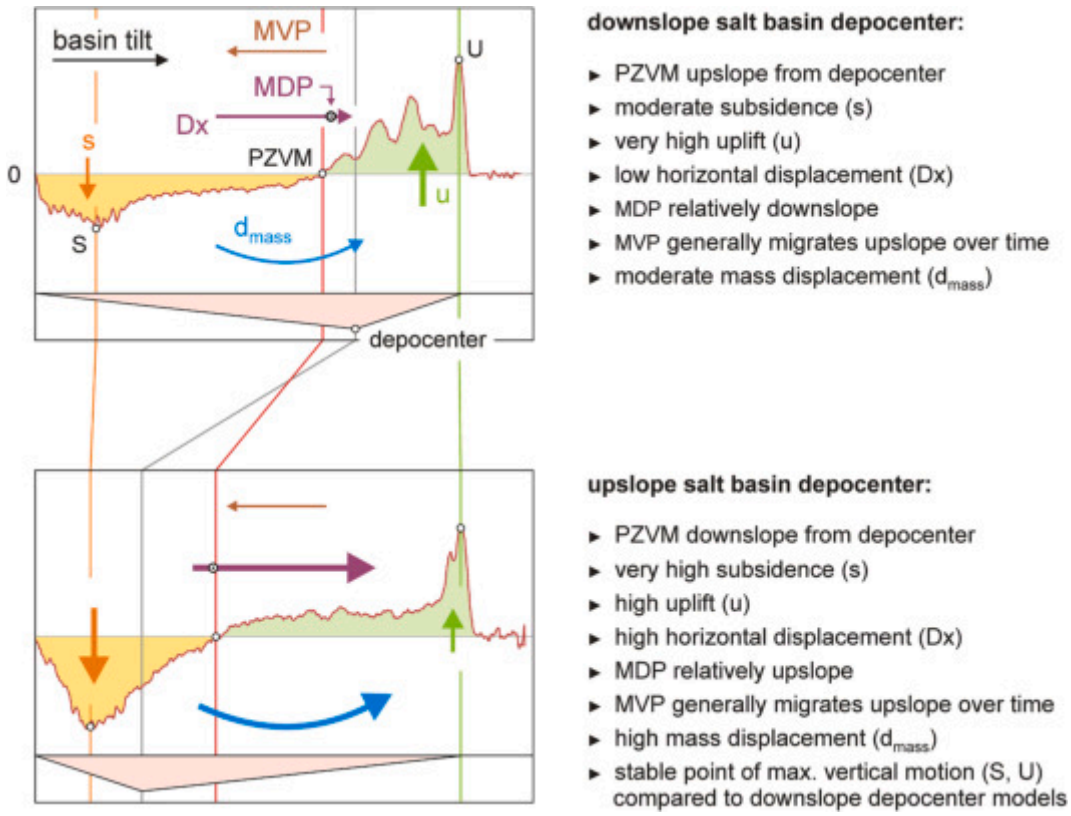


**Fig. 13.** Impact of basin geometry (grey shape) on salt tectonics from PIV and topographic analysis on Series II experiments K–O (3° basin tilt, constant mean salt thickness). The red curve indicates final model topography along the central model axis, and the orange and green areas indicate the area of subsidence and uplift in profile, respectively. PZVM: point of zero vertical motion, MDP: maximum displacement point, MVP: maximum velocity point. For more details on definitions, see Fig. 3. (For interpretation of the references to color in this figure legend, the reader is referred to the Web version of this article.)

downslope (e.g. Brun and Fort, 2011; Peel, 2014). Yet this effect diminished over time in the experiments, as material moved downslope so that the system ran out of potential energy (i.e. loss of gravitational head) and started to stabilize (yet did not fully settled, and will probably never do so due to basal drag, Fig. 12e), as is consistent with the instant titling boundary condition (Ge et al., 2019b).

The second important factor in our experiments is mean salt thickness, which itself is a general constraint based on the basin's geometry (i.e. the general salt basin depth) and the available volume of salt in a system. The thicker the overall salt layer, the less stable the system is when it starts to tilt due to reduced shear strength and consequent reduced coupling with the base of the basin (e.g. Brun and Fort, 2011).

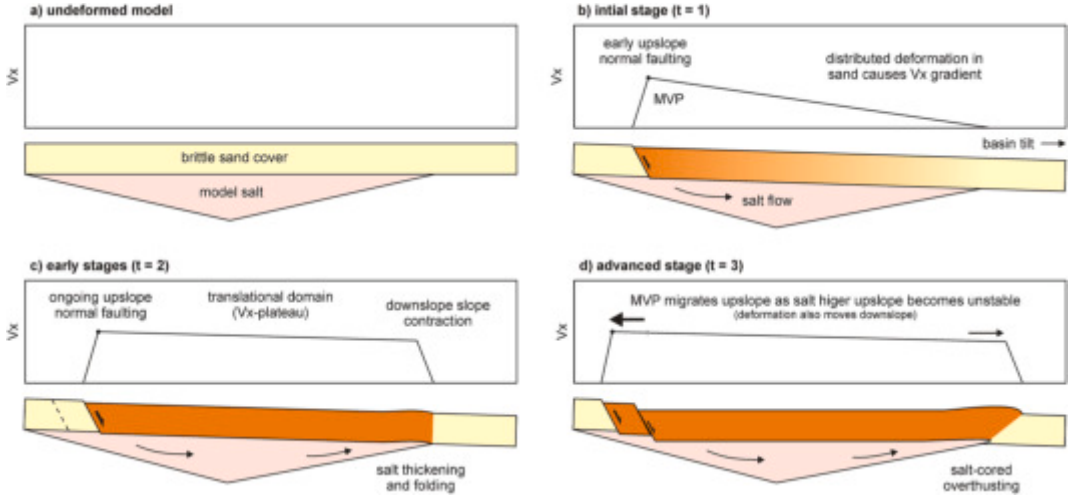


**Fig. 14.** Development of the various domains of a salt tectonic system as derived from the PIV- derived incremental displacement (Vx) profiles shown in Figs. 5, 6, 8 and 10. MVP: maximum velocity point. Red indicates downslope displacement. (For interpretation of the references to color in this figure legend, the reader is referred to the Web version of this article.)

Because the viscous nature of the model salt (i.e. the PDMS silicone), its strength is directly related to forces driving its deformation and the resulting shear rate. Thicker salt layers under constant gravitational forces are therefore weaker because shear is more distributed and shear rates consequently lower.

### 4.2. Influence of salt basin depocenter location

Although basin tilt and mean salt thickness dominate our model results, the experiments with a constant mean salt thickness and 3° basin tilt (Models K–O) allow us to assess the secondary effects of basin shape (i.e. depocenter location) on salt tectonics (summarized in Fig. 13).

On a large scale, we found a decrease in total mass displacement when the salt basin depocenter is shifted downslope (Figs. 7 and 11b). The same correlation exists between total cumulative displacement and salt basin depocenter location, supporting this observation (Figs. 8 and 12c, d). The fact that cumulative displacement decreased when the salt basin depocenter was situated more downslope is likely linked to the associated distribution of potential energy in the system; the higher upslope the depocenter is situated, the more (unstable viscous) material is available upslope, the pressure of which more readily overcomes basal drag, causing enhanced downslope displacement and subsidence in the upslope parts (Figs. 1, 7 and 8, 11b and 12c, d).

A more upslope salt basin depocenter location is also strongly associated with the PZVM and MDP sitting higher upslope (Figs. 11e, 12f and 13). This trend is accompanied by an increase in maximum subsidence in the upslope extension domain, made possible by the increased thickness of the salt basin there, which can be readily evacuated to leave more space for subsequent subsidence (e.g. Dooley et al., 2017; Pichel et al., 2018, Fig. 11c). We simultaneously found less localized uplift (lower maximum uplift values) in the downslope domain (Fig. 11c), but the increased mass displacement caused a wider, more general uplift there (Figs. 7 and 13). This was because when the depocenter was higher upslope, the downslope part of the basin became relatively shallow. As a result, the thinner salt analogue did not allow deformation in the brittle layer due to increased brittle-viscous coupling and basal drag, causing a wider thickening and uplift (similar to the models by Dooley et al., 2017 and Pichel et al., 2018).

Basal drag may have caused the PZVM shift in models U–W as well (Fig. 9a–c, 10a-i), even though these models also had varying mean salt thicknesses that likely affected the results. The braking effect of basal drag was also clearly seen in experiments with a maximum 5 mm basin depth (Fig. 9d and e, 10j-o), and was the reason for the decreased propagation of deformation out of the basin in Models K–O when the depocenter was situated higher upslope, since the brittle cover was less effective in moving over the thinner viscous layer downslope (e.g. Dooley et al., 2017, 2018, Fig. 13).

A further insight from the topography analysis is that the translational domain, which moved without significant internal horizontal deformation, did actually tilt due to upslope subsidence and downslope uplift (Fig. 7). This contrast was so significant that the sand cover in the translational domain “buckled”, as observed in Models L-N (Fig. 7b–d). Both horizontal and vertical translational motions are thus clearly accommodated by the deforming viscous layer below. The exact expression of this “buckling” or “contractional hinge” (Jackson and Hudec, 2017) seems to have been a factor of salt basin depocenter location as thinner downslope salt thicknesses caused increased basal drag and wider uplift zones (Fig. 13).

Also, the location of maximum uplift and subsidence remained rather stable (Figs. 11d and 13). The point of maximum uplift was always situated near the downslope end of the salt basin, downslope of which deformation was almost impossible. Downslope migration of the maximum subsidence point was probably prohibited by the relatively stable translational domain, as the downslope motion of this domain was controlled by the contraction at the downslope edge of the basin. Yet these insights represent the final model state and we may expect some slight variations over time, although the general trend we observed most likely remains valid.

A final point of attention is that displacement was anomalously high in both Models C and M with salt basin shape 3 (Fig. 5i–g, 7c, 8i-g, 11b-e, 12c and d). The fact that this occurred in two models might indicate that it was probably no strange discrepancy due to for instance model preparation. Perhaps basin shape 3 was close to the optimal basin shape for accommodating gravity-gliding type salt tectonics. The salt thickness on both sides of the salt basin depocenter in this basin geometry was relatively high, but the slight upslope depocenter location would then still have allowed for relatively high degrees of instability.

### 4.3. Development of salt tectonic domains

Most of our models developed the distinct gravity-gliding domains typical for gravity-gliding systems (i.e. upslope extension, mid-slope translation and downslope contraction, e.g. Demercian et al., 1993; Spathopolous, 1996; Rowan et al., 2004; Brun and Fort, 2011; Dooley et al., 2017). Yet these domains were generally not established during the initial phases of our models, as expressed by the initial bell-shape of the Vy-profiles, and in some of the 1° basin tilt models from Series I, they did not develop at all (Figs. 5, 6, 8 and 10).

We propose that the brittle sand layer covering the salt basin stabilized the system as it formed a brittle seal with finite yield strength that prevented immediate deformation due to salt instability as the basin was (slightly) tilted (Ritter et al., 2018, compare to Series III models without sand cover in the Appendix). In our 1° margin tilt experiments this stabilizing effect seems to have largely balanced the gravitational forces, allowing only limited deformation to occur (Fig. 4a and b, 5, 6). Yet in the 3° basin tilt models, gravitational forces readily overcame the peak strength of the sand layer, enabling the development of the typical salt-tectonic domains (Fig. 4c and d, 7-10).

The Vx results reveal how this establishment of the salt tectonic system occured in more detail (Fig. 14). Initially, the tilting of the basin caused displacement without a clear plateau and the highest displacements situated upslope, where extensional faulting occurs. However, no sufficient force was yet available to cause contractional deformation in the downslope part of the salt basin, hence the decrease in displacement towards the downslope end of the salt basin (Fig. 14b). As upslope displacement continued, sufficient stress built up to induce contraction in the downslope domain. As a result, a translational domain with near-constant displacement could be established (Fig. 14c). Subsequently, as material moved downslope, the parts of the upslope domain that were previously supported by the now fully mobile sand cover of the translational domain became unstable as well, causing an upslope shift in maximum displacement rates (i.e. the MVP migrates upslope, Figs. 12g and 14d). Next to this inferred support by the translational domain, basal drag at the upslope part of the salt basin probably decelerated downslope salt flow there as well, contributing to the delayed extension captured in our Vx plots (Dooley et al., 2017). Similar migration of displacement patterns was also observed in models by Quirk et al. (2012) and Ge et al. (2019b).

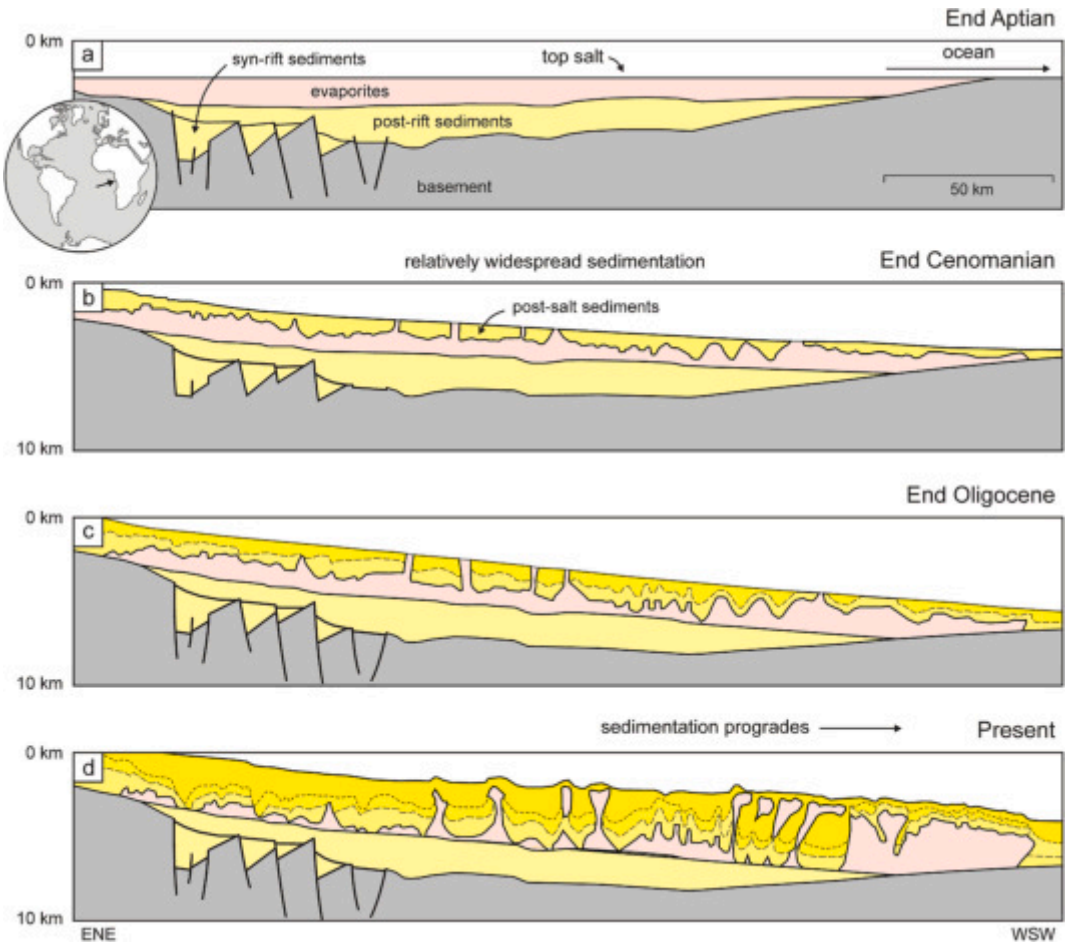


**Fig. 15.** Evolution of the Lower Congo Basin after evaporite deposition in a basin with a relatively downslope depocenter. Modified after Marton et al. (2000). Dotted lines indicate the top of the sediments from the previous stage(s).

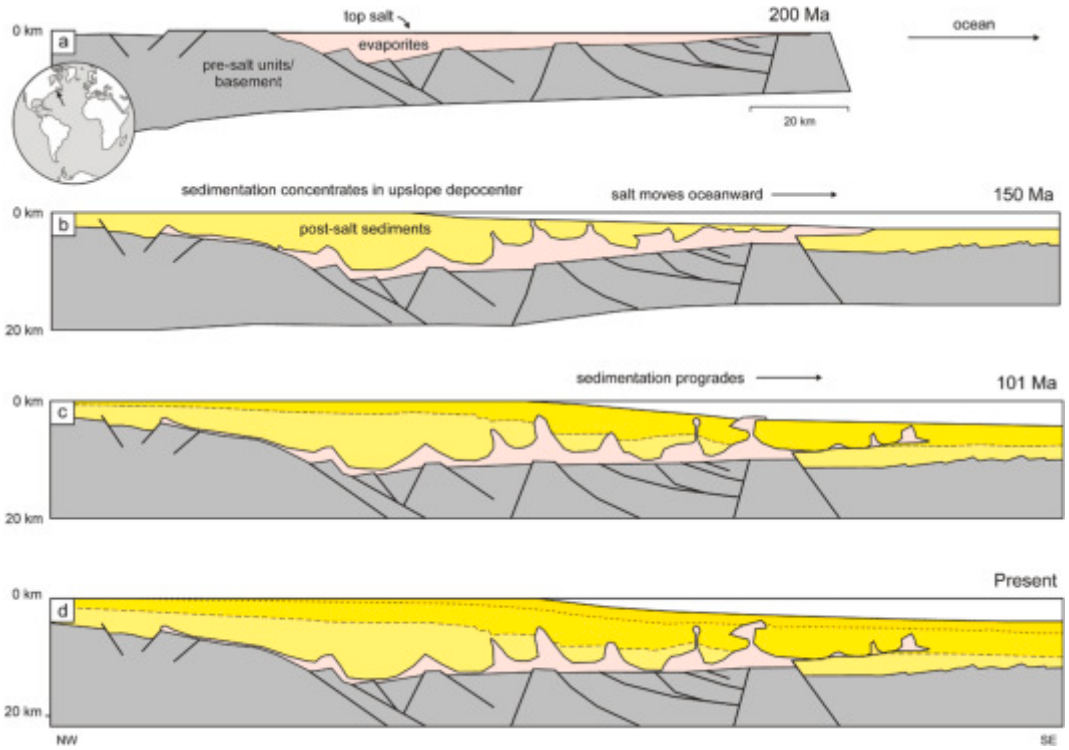


**Fig. 16.** Evolution of the Scotian Margin (Section NS, 2000) after salt deposition in a basin with an upslope depocenter. Modified after PFA (2011). Dotted lines indicate the top of the sediments from the previous stage(s).

Finally, in some models, we observed a late downslope migration of the MVP (Fig. 12g). This may have been due to the eventual exhaustion of mobile model salt in the upslope domain, so that further deformation could only occur farther downslope.

### 4.4. Model limitations

Although our simple model set-up allows us to extract a number useful insights into the effects of basin tilt and salt basin geometry (i.e. mean salt thickness and depocenter location), some limitations exist that need to be taken into account.

Firstly, the basin tilt we applied in our models was instantaneous, whereas margin tilt due to differential thermal subsidence along a passive margin is considered to be gradual. Although instantaneous basin tilting has often been used in previous modelling studies (e.g. Brun and Fort, 2004, Fort et al., 2004a, b, Quirk et al., 2012; Dooley et al., 2018), the application of a gradual basin tilt might have been more realistic (e.g. Ge et al., 2019a, b; Warsitzka et al., 2021). However, our modelling results show that small degrees of tilting do only cause very limited deformation and most deformation takes place when tilt angles are higher. Therefore the discrepancy between natural examples and our models is probably less distinct than might appear. One could even use the 1° basin tilt models from our Series I as an example of early state salt tectonic deformation along a young passive margin, and the 3° basin tilt models to interpret structures in more mature systems.

Another limitation concerns the lack of syn-kinematic (or post-salt) sedimentation. Syn-kinematic sedimentation is generally considered to accelerate or even dominate downslope displacements in salt tectonic systems (e.g. Fort et al., 2004b; Peel, 2014), although in some cases it might have the opposite effect and stabilize a salt tectonic system. Such stabilization may occur when sedimentation is concentrated downslope of the salt basin in question (Warzitska et al., 2021), or when such thick overburdens are accumulated sufficiently fast that the instability of the salt units is not sufficient to cause deformation (Hudec and Jackson, 2007). Either way, our models did contain no syn-kinematic sedimentation and are thus not fully appropriate for interpreting (the more evolved stages of) sediment-rich salt tectonic systems (Goteti et al., 2013).

A final limitation is linked to the length of salt basins; as pointed out by Brun and Fort (2008, 2011), and Tari and Jabour (2013), the length of an evaporite basin has an important influence on its stability as well. When increasing the width of a salt basin, the necessary degree of margin inclination (angle α, Fig. 2c) strongly decreases (Brun and Fort, 2011). Indeed, small isolated basins are known to only allow moderate deformation (Tari and Jabour, 2013), perhaps illustrated by our experiments as well, since deformation only occurs above the viscous layer, limiting the system to the extent of salt basin. Since our models have a constant length of 60 cm, the observed influence of different salt thicknesses represents only part of the parameter space.

### 4.5. Comparison with natural examples

A direct comparison between our generic models and natural examples of salt tectonic systems is challenging due to various factors. First, the exact initial geometry of salt basins is often debatable, as the quality of structural reconstructions is affected by the ductile evaporite behavior and the significant lateral displacements occurring in such systems (e.g. Marton et al., 2000). Furthermore, salt basin geometries can vary greatly along passive margins (e.g. Marton et al., 2000; PFA, 2011; Guerra and Underhill, 2012; Deptuck and Kendell, 2017), and initial gravity-gliding structures may be overprinted by large prograding sedimentary systems that dominate the margins in later stages (e.g. Peel, 2014). Nevertheless, we here present two end member examples that have reasonably well constrained parameters, (the Lower Congo Basin and the Scotian Margin, Figs. 15 and 16), which we compare to our experiments with constant mean salt thickness models and 3° basin tilt.

The Lower Congo Basis is situated on the Atlantic margin of Angola, which started separating from its Brazilian conjugate in the Early Cretaceous (e.g. Fairhead and Wilson, 2005; Heine et al., 2013, and references therein). During the final stages of break-up in the Aptian, marine transgression led to the formation of extensive evaporite deposits in sag basins on both margins (e.g. Davison, 2007). In the Lower Congo Basin, the depocenter of this sag basin was situated rather downslope (Marton et al., 2000, Fig. 15a). As the margin tilted oceanward, the salt became unstable and formed the classical salt tectonic domains that we also observe in our models (Spathopoulos, 1996; Valle et al., 2001, Fig. 15b). Importantly however, is the fact that sedimentation in these early phases was broadly distributed (Marton et al., 2000, Fig. 15b and c), which fits the observation that upslope topography variations are rather gradual in our experiments with downslope depocenters (Fig. 13). Such a bathymetry allowed for widespread sedimentation in the natural example (Fig. 15b and c), until the influx of large amounts of sediments from the Congo Fan prograded into the system (Fig. 15d) making further comparisons impractical.

An example of a salt basin with upslope depocenter is found along the Scotian Margin, at section NS 2000, offshore Canada (Fig. 16). Here, large Triassic salt units were deposited at the end of the opening of the Central Atlantic and subsequently tilted (PFA, 2011; Biari et al., 2017). As a result, post-salt units started to move downslope, synchronously creating most accommodation space higher upslope, similar to our models (Fig. 13), allowing for the subsequent deposition of thicker sedimentary infill there (Fig. 16b). Also in this natural case, large-scale sedimentation eventually caught up and started controlling the system (PFA, 2011, Fig. 16d). It may however be noted that some authors propose sedimentation to be the main driving force during the whole salt tectonic evolution of the margin (Albertz and Beaumont, 2010; Albertz et al., 2010), and that considerable variations in salt basin geometry occur along the Scotian margin (e.g. PFA, 2011; Deptuck and Kendell, 2017).

Our results fit reasonably well with the presented natural examples; although syn-tectonic sedimentation is not directly incorporated in our experiments (see section 4.4), we see a fair correlation between post-salt accommodation space generation in model and nature as a function of salt basin depocenter location (i.e. the loci of thickest, more mobile salt layers). Yet we must perhaps stress that the dominant mechanism controlling salt tectonics on passive margins (i.e. dominant spreading due to sedimentary loading vs. dominant gliding due to margin tilt) is still debated (e.g. Schultz-Ela, 2001; Brun and Fort, 2011, 2012; Rowan et al., 2012; Goteti et al., 2013; Peel, 2014; Warren, 2016). However, even if gravity spreading could arguably be the dominant mechanism in some cases (e.g. in the Santos Basin offshore Brazil, Jackson et al., 2015), we should still expect a very similar relationship between evaporite depocenters and subsequent sedimentation patterns; in both scenarios, the salt is evacuated and replaced by post-salt deposits.

## 5. Conclusion

Our analogue modelling efforts to study the effects of evaporite (salt) basin geometry on gravity-gliding style salt tectonics leads us to the following conclusions:

- An assessment of the whole model population shows that first the degree of basin tilt, followed by the mean salt thickness are dominant factors controlling deformation. The more a basin is tilted and the thicker the salt layer, the more deformation occurs. The salt layer thickness itself is partially a result of basin geometry (in combination with the available volume of salt deposits in the system).
- By focusing on a subpopulation of models with constant mean salt thickness and a 3° tilt, we cancel out the effects of basin tilt and mean salt thickness to isolate the influence of basin geometry, i.e. depocenter location. In these experiments, we find that the location of the

salt basin depocenter has various effects on the distribution and expression of tectonic domains in a salt tectonic system (Fig. 13).

- When the depocenter is situated downslope, upslope subsidence is moderate, as the downslope displacement of material is limited by the relatively low gravitational potential in the system. Yet the downslope presence of abundant viscous material allows significant localized uplift there. The main depocenter being situated higher upslope causes deformation to occur higher upslope as well, concentrating upslope subsidence allowed by the thicker model salt there, while distributing downslope uplift due to the thinner model salt and increased basal drag prevented significant displacements. Also the increased instability due to larger volumes of viscous material sitting higher upslope, means that there is an increase in downslope displacement.
- When comparing our model results with natural examples from Atlantic passive margins, we find a fair correlation expressed in the links between salt depocenter location and subsequent sedimentation patterns. When the salt depocenter is situated upslope, salt evacuation will localize accommodation space generation and post-salt deposition in the upslope part of the system. By contrast, a downslope salt depocenter allows the generation of more distributed accommodation space and sedimentation. These insights should be applied to interpret the early stages of salt tectonic deformation along passive margins, as during later stages, sedimentary loading might become the dominant driving factor.

## Data availability

Supplementary material involving PIV analysis results, digital topography maps and original measurements are combined in a GFZ data publication (Zwaan et al., 2021), which is publicly accessible via the following link: https://doi.org/10.5880/fidgeo.2021.028.

## CrediT author statement

**Frank Zwaan:** Conceptualization, Methodology, Investigation, Writing – Original Draft, Formal Analysis, Validation, Data Curation, Visualization, Project Administration. **Matthias Rosenau:** Formal Analysis, Data Curation, Visualization, Writing - Review & Editing. **Daniele Maestrelli:** Formal Analysis, Data Curation, Visualization, Writing - Review & Editing.

## Declaration of competing interest

The authors declare that they have no known competing financial interests or personal relationships that could have appeared to influence the work reported in this paper.

## Acknowledgements

We are grateful to the Géosciences, CNRS analogue modelling laboratory at Université de Rennes 1, France, (Jean-Jacques Kermarrec and Pascal Roland) for providing access to the laboratory facilities and for technical support. We warmly thank editor Tiago Alves, and reviewers Tim Dooley and Juan I. Soto for their detailed and constructive feedback that greatly helped to improve the paper. The University of Bern is acknowledged for covering the Open Access publication costs, and we are grateful to Kirsten Elger for archiving the supplementary material associated with this paper in the form of a GFZ data publication (Zwaan et al., 2021).

## Appendix A. Results from models without sand cover (series III)

Next to the models of Series I and II, which included a brittle sand cover to simulate post-salt sediments, we also completed a third series of models without such a brittle cover. All ten of these Series III models (Z1-Z10) involved a 3° basin tilt. Similar to Series I and II models, we found that the mean model salt thickness has a strong influence on subsequent deformation. Hence we include only the results of the topography and PIV analysis of Models Z1-Z5, highlighting the influence of the model salt basin depocenter, as well as the other characteristics typical of a hypothetical salt tectonic system without post-salt units. The results of the additional models Z6-Z10 can be found in the supplementary material (Zwaan et al., 2021).

### *A1. Topographic analysis results of Models Z1-Z5*

The final normalized topography of Models Z1-Z5 is presented in Fig. A1. In contrast to the typical salt tectonic domains found in Series II models (Figs. 7 and 9), Models Z1-Z5 formed a much more gradual relief. This type of topography in the absence of a brittle cover was also obtained in the numerical models by Quirk et al., (2012) and Goteti et al., (2013). However, similar to their equivalents from Series II (Models K-O), a downslope model salt basin depocenter led to the PZVM being situated higher upslope, as well as to a decrease in maximum downslope uplift and an increase in upslope subsidence (Fig. 7, A1). This was likely for the same reasons as in Series II models: basal drag prevented downslope motion in basins with relative thin salt layers in the downslope domain, and hampered the evacuation of viscous material from upslope salt basin depocenters. A difference with the Series II models was that both the PMU and PMS followed the same trend as the PZVM in Models Z1-Z5, instead of remaining relatively stable, and that the total mass displacement remained rather constant in Models Z1-Z5. This was likely because the absence of a brittle layer allowed the model salt maximal freedom to adjust to the tilted basin state.

### *A2. PIV analysis results of Models Z1-Z5*

The PIV results of our 3° tilt models Z1-Z5 without sand cover are illustrated in Figs. A2 and A3. Where the equivalent experiments with sand cover developed clear plateau-shaped displacement curves representing the typical salt tectonic domains (Fig. 8), the PIV analysis produced much smoother, almost bell-shaped displacement curves for Models Z1-Z5. These curves represented a distributed extensional domain upslope merging with a distributed downslope compressional domain, and the peak displacement being located in between (Fig. A2). Cumulative displacement (Dxmax) values were slightly lower in equivalent Models K–O from Series II, and increased as the model salt basin depocenter was situated higher upslope (from 45 mm in Model Z1 to 58 mm in Model Z5). This lower maximum cumulative displacement with respect to Models K–O was probably due to the absence of mass in the form of a sand cover accelerating deformation. Another effect of the model salt depocenter location are the differences in MVP evolution (Fig. A3). As seen in the models with sand cover in the main text, displacement rates were highest during the initial phases and decreased towards the end of the model run, yet we also found that the MVP either migrated upslope or downslope, depending on the location of the model salt basin depocenter. We speculate that this was related to the bulge-shape of the surface deformation; the MVP might represent the crest of the bulge, which may move downslope fast if material flows out of an upslope salt basin depocenter, or which may be stalled in the opposite situation.

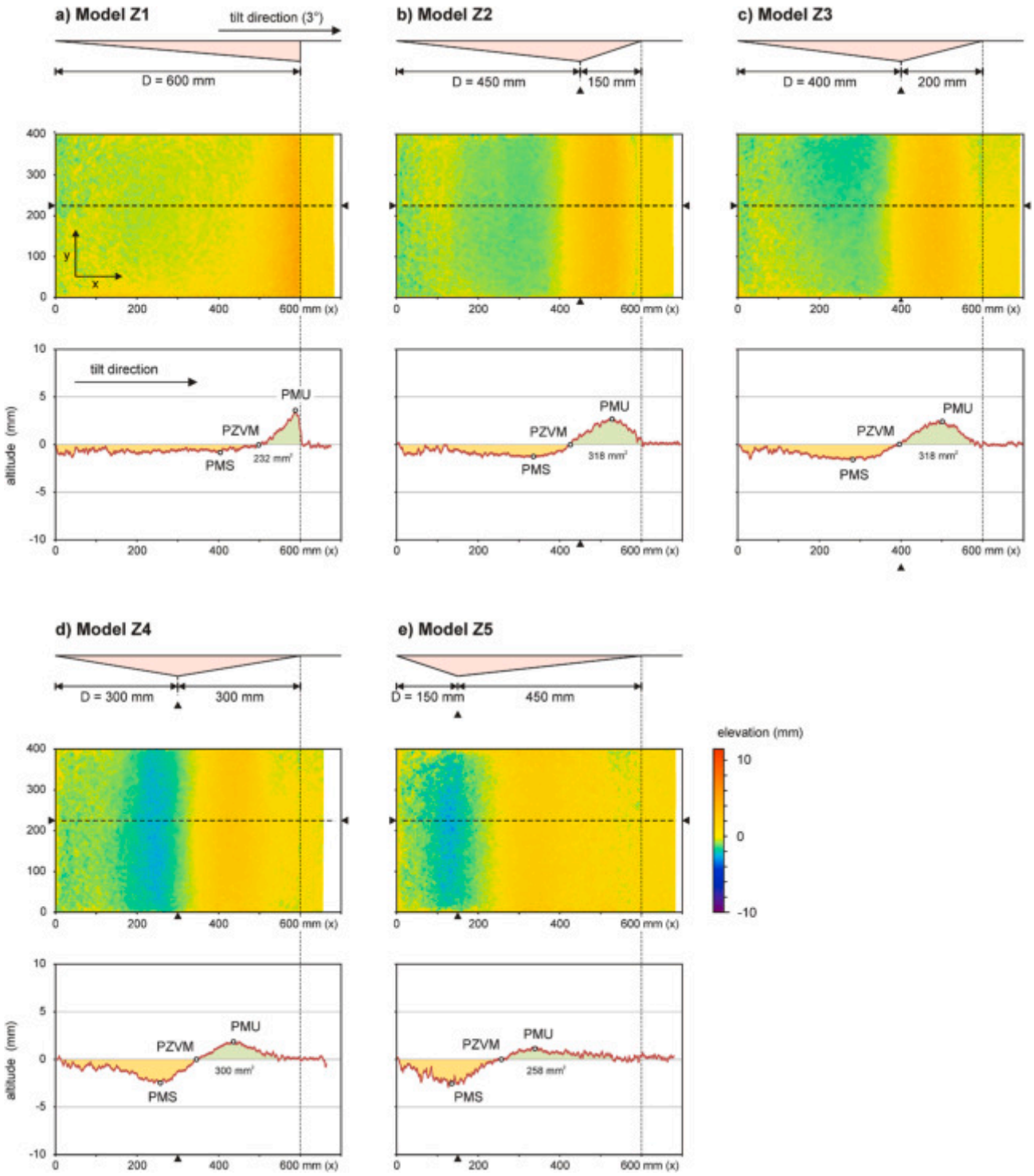


**Fig. A1.** Final normalized topography of Models Z1-Z5 from Series III (3° basin tilt, basin shapes 1–5 with constant mean salt thickness, but no sand cover) in map view and along a central section. PZVM: point of zero vertical motion, PMS: point of maximum subsidence, PMU: point of maximum uplift. For more details on definitions, see Fig. 3.

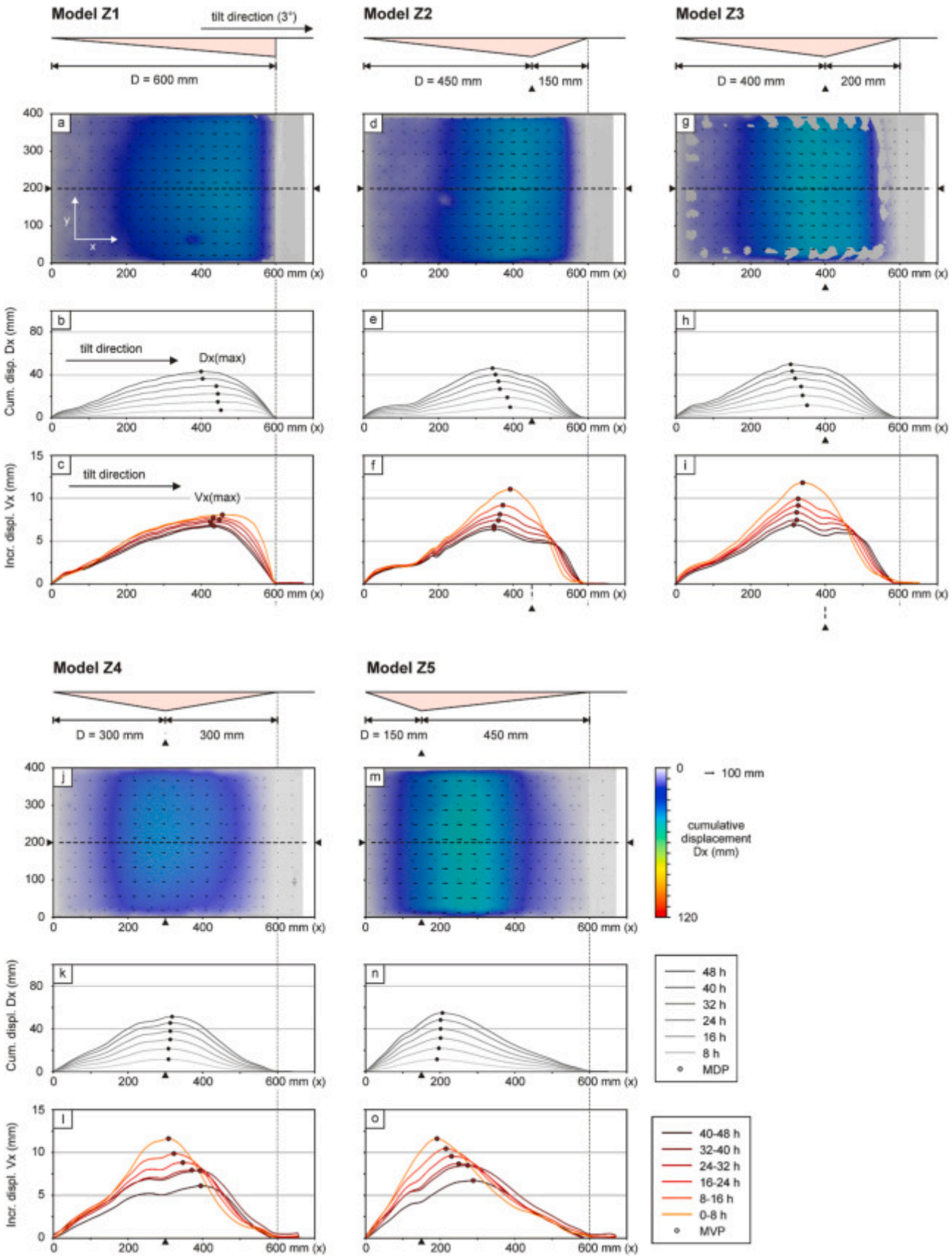


**Fig. A2.** PIV-derived surface displacements of models Z1-Z5 from Series III (3° basin tilt, basin shapes 1–5, with constant mean salt thickness, but no sand cover), shown in both map view (Dx only) and plotted on along-axis profiles (both Dx and Vx). MDP: maximum displacement point. MVP: maximum displacement point. For more details on definitions, see Fig. 3.

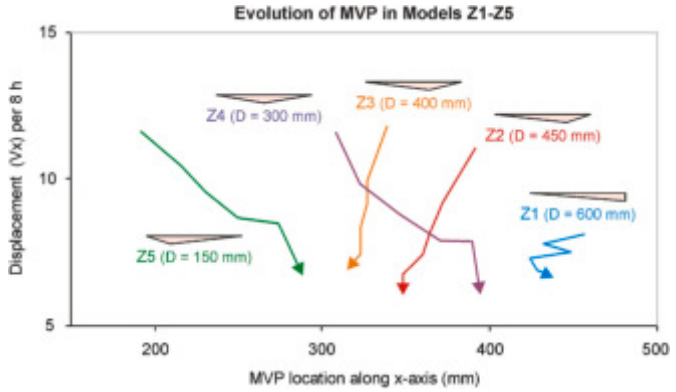


**Fig. A3.** Evolution of the maximum velocity point or MVP (location and associated $Vy_{max}$) over time for Models Z1-Z5. The arrows indicate the direction of evolution.

## References


Adam, J., Urai, J.L., Wieneke, B., Oncken, O., Pfeiffer, K., Kukowski, N., Lohrmann, J., Hoth, S., van der Zee, W., Schmatz, J., 2005. Shear localisation and strain distribution during tectonic faulting - new insights from granular-flow experiments and high-resolution optical image correlation techniques. J. Struct. Geol. 27, 183–301. https://doi.org/10.1016/j.jsg.2004.08.008.

Adam, J., Krezsek, C., 2012. Basin-scale salt tectonic processes of the Laurentian Basin, Eastern Canada: insights from integrated regional 2-D seismic interpretation and 4D physical experiments. In: Alsop, G.I., Archer, S.G., Hartley, A.J., Grant, N.T., Hodgkinson, R. (Eds.), Salt Tectonics, Sediments and Prospectivity. Geol. Soc. Lond. Spec. Publ. 363, 331–360. https://doi.org/10.1144/SP363.15.

Albertz, M., Beaumont, C., 2010. An investigation of salt tectonic structural styles in the Scotian Basin, offshore Atlantic Canada: 2. Comparison of observations with geometrically complex numerical models. Tectonics 27, TC4018. https://doi.org/10.1029/2009TC002540.

Albertz, M., Beaumont, C., Shimeld, J.W., Ings, S.J., Gradmann, S., 2010. An investigation of salt tectonic structural styles in the Scotian Basin, offshore Atlantic Canada: 1. Comparison of observations with geometrically simple numerical models. Tectonics 29, TC4017. https://doi.org/10.1029/2009TC002539.

Allen, J., Beaumont, C., 2012. Impact of inconsistent density scaling on physical analogue models of continental margin scale salt tectonics. J. Geophys. Res. 117, B08103. https://doi.org/10.1029/2012JB009227.

Allen, J., Beaumont, C., 2015. Continental margin syn-rift salt tectonics at intermediate width margins. Basin Res. 28, 598–633. https://doi.org/10.1111/bre.12123.

Biari, Y., Klingelhoefer, F., Sahabi, M., Funck, T., Benabdellouahed, M., Schnabel, M., Reichert, C., Gutscher, M.-A., Bronner, A., Austin, J.A., 2017. Opening of the central Atlantic Ocean: implications for geometric rifting and asymmetric initial seafloor spreading after continental breakup. Tectonics 36, 1129–1150. https://doi.org/10.1002/2017TC004596.

Bonatti, E., Emiliani, C., Ostlund, G., Rydell, H., 1971. Final desiccation of the Afar rift, Ethiopia. Science 172, 468–469. https://doi.org/10.1126/science.172.3982.468.

Boutelier, D., Schrank, C., Regenauer-Lieb, K., 2019. 2-D finite displacements and strain from particle imaging velocimetry (PIV) analysis of tectonic analogue models with TecPIV. Solid Earth 10, 1123–1139. https://doi.org/10.5194/se-10-1123-2019.

Brun, J.-P., Fort, X., 2004. Compressional salt tectonics (Angolan margin). Tectonophysics 382, 129–150. https://doi.org/10.1016/j.tecto.2003.11.014.

Brun, J.-P., Fort, X., 2008. Entre sel et terre. Structures et mécanismes de la tectonique salifère. Collection Interactions, Vuibert, Paris. https://hal-insu.archives-ouvertes.fr/insu-00334744.

Brun, J.-P., Fort, X., 2011. Salt tectonics at passive margins: geology versus models. Mar. Petrol. Geol. 28, 1123–1145. https://doi.org/10.1016/j.marpetgeo.2011.03.004.

Brun, J.-P., Fort, X., 2012. Salt tectonics at passive margins: geology versus models – Reply. Mar. Petrol. Geol. 37, 195–208. https://doi.org/10.1016/j.marpetgeo.2012.04.008.

Cobbold, P.R., Szatmari, P., 1991. Radial gravitational gliding on passive margins. Tectonophysics 188, 249–289. https://doi.org/10.1016/0040-1951(91)90459-6.

Cobbold, P., Rosello, E., Vendeville, B., 1989. Some experiments on interacting sedimentation and deformation above salt horizons. Bull. Soc. Geol. Fr. 3, 453–460. https://doi.org/10.2113/gssgfbull.V.3.453.

Davison, I., 2007. Geology and tectonics of the South Atlantic Brazilian. In: Ries, A.C., Butler, R.W.H., Graham, R.H. (Eds.), Deformation of the Continental Crust: the Legacy of Mike Coward. Geol. Soc. Lond. Spec. Publ. 272, 345–359. https://doi.org/10.1144/GSL.SP.2007.272.01.18.

Davison, I., Anderson, L., Nutall, P., 2012. Salt deposition, loading and gravity drainage in the Campos and Santos salt basins. In: Alsop, G.I., Archer, S.G., Hartley, A.J., Grant, N.T., Hodgkinson, R. (Eds.), Salt Tectonics, Sediments and Prospectivity. Geol. Soc. Lond. Spec. Publ. 363, 159–173. https://doi.org/10.1144/SP363.8.

Demercian, S., Szatmari, P., Cobbold, P.R., 1993. Style and pattern of salt diapirs due to thin-skinned gravitational gliding, Campos and Santos basins, offshore Brazil. Tectonophysics 3–4, 393–433. https://doi.org/10.1016/0040-1951(93)90351-J.

Deptuck, M.E., Kendell, K.L., 2017. A Review of Mesozoic-Cenozoic Salt Tectonics Along the Scotian Margin, Eastern Canada. In: Soto, J.I., Flinch, J.F., Tari, G. (Eds.), Permo-Triassic Salt Provinces of Europe, North Africa and the Atlantic Margins. Elsevier, pp. 287–312. https://doi.org/10.1016/B978-0-12-809417-4.00014-8.

Dooley, T.P., Hudec, M.R., 2017. The effects of base-salt relief on salt flow and suprasalt deformation patterns — Part 2: application to the eastern Gulf of Mexico. Interpretation 5, SD25–SD38. https://doi.org/10.1190/INT-2016-0088.1.

Dooley, T.P., Hudec, M.R., Carruthers, D., Jackson, M.P.A., Luo, G., 2017. The effects of base-salt relief on salt flow and suprasalt deformation patterns — Part 1: flow across simple steps in the base of salt. Interpretation 5, SD1–SD23. https://doi.org/10.1190/INT-2016-0087.1.

Dooley, T.P., Hudec, M.R., Pichel, L.M., Jackson, M.P.A., 2018. The impact of base-salt relief on salt flow and suprasalt deformation patterns at the autochthonous, paraautochthonous and allochthonous level: insights from physical models. In: McClay, K.R., Hammerstein, J.A. (Eds.), Passive Margins: Tectonics, Sedimentation and Magmatism. Geol. Soc. Lond. Spec. Publ. 476, 287–315. https://doi.org/10.1144/SP476.13.

Fairhead, J.D., Wilson, M., 2005. Plate tectonic processes in the South Atlantic Ocean: do we need deep mantle plumes?. In: Foulger, G.R., Natland, J.H., Presnall, D.C., Anderson, D.L. (Eds.), Plates, Plumes, and Paradigms. Geol. Soc. Am. Spec. Paper 388, 533–537. https://doi.org/10.1130/0-8137-2388-4.537.

Ferrer, O., Gratacós, O., Roca, E., Muñoz, J.A., 2017. Modeling the interaction between presalt seamounts and gravitational failure in salt-bearing passive margins: the Messinian case in the northwestern Mediterranean Basin. Interpretation 5, SD99–SD117. https://doi.org/10.1190/INT-2016-0096.1.

Fort, X., Brun, J.-P., Chauvel, F., 2004a. Salt tectonics on the Angolan margin, synsedimentary deformation processes. AAPG Bull. 88, 1523–1544. https://doi.org/10.1306/06010403012.

Fort, X., Brun, J.-P., Chauvel, F., 2004b. Contraction induced by block rotation above salt (Angolan margin). Mar. Petrol. Geol. 21, 1281–1294. https://doi.org/10.1016/j.marpetgeo.2004.09.006.

Garcia, S.F.M., Letouzey, J., Rudkiewicz, J.-L., Filho, A.D., Frizon de Lamotte, D.F., 2012. Structural modeling based on sequential restoration of gravitational salt deformation in the Santos Basin (Brazil). Mar. Petrol. Geol. 35, 337–353. https://doi.org/10.1016/j.marpetgeo.2012.02.009.

Gaullier, V., Brun, J.-P., Guérin, G., Lecanu, H., 1993. Raft tectonics: the effects of residual topography below a salt décollement. Tectonophysics 228, 363–381. https://doi.org/10.1016/0040-1951(93)90349-O.

Gaullier, V., Vendeville, B.C., 2005. Salt tectonics driven by sediment progradation. Part II: radial spreading of sedimentary lobes prograding above salt. AAPG Bull. 89, 1081–1089. https://doi.org/10.1306/03310503064.

Ge, Z., Rosenau, M., Warsitzka, M., Gawthorpe, R.L., 2019a. Overprinting translational domains in passive margin salt basins: insights from analogue modelling. Solid Earth 10, 1283–1300. https://doi.org/10.5194/se-10-1283-2019.

Ge, Z., Warsitzka, M., Rosenau, M., Gawthorpe, R.L., 2019b. Progressive tilting of salt-bearing continental margins controls thin-skinned deformation. Geology 47, 1122–1126. https://doi.org/10.1130/G46485.1.

Gemmer, L., Ings, S.J., Medvedev, G., Baumont, C., 2004. Salt tectonics driven by differential sediment loading: stability analysis and finite-element experiments. Basin Research 16, 199–218. https://doi.org/10.1111/j.1365-2117.2004.00229.x.

Gemmer, L., Beaumont, C., Ings, S.J., 2005. Dynamic modelling of passive margin salt tectonics: effects of water loading, sediment properties and sedimentation patterns. Basin Res. 17, 383–402. https://doi.org/10.1111/j.1365-2117.2005.00274.x.

Goteti, R., Beaumont, C., Ings, S.J., 2013. Factors controlling early stage salt tectonics at rifted continental margins and their thermal consequences. J. Geophys. Res.: Solid Earth 118, 3190–3220. https://doi.org/10.1002/jgrb.50201.

Guerra, M.C.M., Underhill, J.R., 2012. Role of halokinesis in controlling structural styles and sediment dispersal in the Santos Basin, offshore Brazil. In: Alsop, G.I., Archer, S. F. Zwaan et al. G., Hartley, A.J., Grant, N.T., Hodgkinson, R. (Eds.),. Salt Tectonics, Sediments and Prospectivity. Geol. Soc. Lond. Spec. Publ. 363, 175–206. https://doi.org/10.1144/SP363.9.

Heine, C., Zoethout, J.M., Müller, R.D., 2013. Kinematics of the South Atlantic rift. Solid Earth 4, 215–253. https://doi.org/10.5194/se-4-215-2013.
Hubbert, M.K., 1937. Theory of scaled models as applied to the study of geological structures. Geol. Soc. Am. Bull. 48, 1459–1520. https://doi.org/10.1130/GSAB-48-1459.
Hudec, M.R., Jackson, M.P.A., 2006. Advance of allochthonous salt sheets in passive margins and orogens. AAPG Bull. 90, 1535–1564. https://doi.org/10.1306/05080605143.
Hudec, M.R., Jackson, M.P.A., 2007. Terra infirma: understanding salt tectonics. Earth Sci. Rev. 82, 1–28. https://doi.org/10.1016/j.earscirev.2007.01.001.
Hudec, M.R., Jackson, M.P.A., 2012. De Re Salica: fundamental principles of salt tectonics. In: Roberts, D.G., Bally, A.W. (Eds.), Regional Geology and Tectonics: Phanerozoic Passive Margins, Cratonic Basins and Global Tectonic Maps. Elsevier, pp. 18–41. https://doi.org/10.1016/B978-0-444-56357-6.00001-9.
Ings, S., Beaumont, C., Gemmer, L., 2004. Numerical modeling of salt tectonics on passive continental margins: preliminary assessment of the effects of sediment loading, buoyancy, margin tilt, and isostasy. In: Post, P.J., Olson, D.L., Lyons, K.T., Palmes, S.L., Harrison, P.F., Rosen, N.C. (Eds.), Salt Sediment Interactions and Hydrocarbon Prospectivity: 24th Annual GCSSEPM Foundation Bob F. Perkins Research Conference Proceedings, pp. 36–68. https://doi.org/10.5724/gcs.04.24.0036.
Jackson, M.P.A., Talbot, 1986. External shapes, strain rates, and dynamics of salt structures. Geol. Soc. Am. Bull. 97, 305–323. https://doi.org/10.1130/0016-7606(1986)97<305:ESSRAD>2.0.CO;2.
Jackson, M.P.A., Hudec, M.R., 2017. Salt Tectonics: Principles and Practice. Cambridge University Press. https://doi.org/10.1017/9781139003988.
Jackson, C.A.-L., Jackson, M.P.A., Hudec, M.R., 2015. Understanding the kinematics of salt-bearing passive margins: a critical test of competing hypotheses for the origin of the Albian Gap, Santos Basin, offshore Brazil. Geol. Soc. Am. Bull. 127, 1170–1751. https://doi.org/10.1130/B31290.1.
Klinkmüller, M., Schreurs, G., Rosenau, M., Kemnitz, H., 2016. Properties of granular analogue model materials: A community wide survey. Tectonophysics 684, 23–38. https://doi.org/10.1016/j.tecto.2016.01.017.
Maillard, A., Gaullier, V., Vendeville, B.C., Odonne, F., 2003. Influence of differential compaction above basement steps on salt tectonics in the Ligurian-Provençal Basin, northwest Mediterranean. Mar. Petrol. Geol. 20, 13–27. https://doi.org/10.1016/S0264-8172(03)00022-9.
Marton, L.G., Tari, G.C., Lehmann, C.T., 2000. Evolution of the Angolan passive margin, West Africa, with emphasis on post-salt structural styles. AGU Geophys. Monogr. Ser. 115, 129–149. https://doi.org/10.1029/GM115p0129.
Mauduit, T., Guerin, G., Brun, J.-P., Lecanu, H., 1997. Raft tectonics: the effects of basal slope angle and sedimentation rate on progressive extension. J. Struct. Geol. 19, 1219–1230. https://doi.org/10.1016/S0191-8141(97)00037-0.
Mauduit, T., Brun, J.-P., 1998. Growth fault/rollover systems: birth, growth, and decay. J. Geophys. Res. 103, 119–136. https://doi.org/10.1029/97JB02484.
McClay, K.R., Dooley, T., Whitehouse, P., Mills, M., 2002. 4-D evolution of rift systems: Insights from scaled physical models. AAPG Bull. 86, 935–959. https://doi.org/10.1306/61EEDBF2-173E-11D7-8645000102C1865D.
Peel, F.J., Travis, C.J., Hossack, J.R., 1995. Genetic structural provinces and salt tectonics of the cenozoic offshore U.S. Gulf of Mexico: a preliminary analysis. In: Jackson, M.P.A.,Roberts, D.G., Snelson, S. (Eds.), Salt Tectonics: A Global Perspective. AAPG Memoir 65, 153–175. https://doi.org/10.1306/M65604C7.
Peel, F.J., 2014. How do salt withdrawal minibasins form? Insights from forward modelling, and implications for hydrocarbon migration. Tectonophysics 630, 222–235. https://doi.org/10.1016/j.tecto.2014.05.027.
PFA (Nova Scotia Play Fairway Analysis Atlas), 2011. Nova Scotia Department of Energy and Mines, Canada. https://energy.novascotia.ca/oil-and-gas/offshore/play-fairway-analysis/analysis.
Pichel, L.M., Peel, F., Jackson, C.A.-L., Huuse, M., 2018. Geometry and kinematics of salt-detached ramp syncline basins. J. Struct. Geol. 115, 208–230. https://doi.org/10.1016/j.jsg.2018.07.016.
Pichel, L.M., Finch, E., Gawthorpe, R.L., 2019. The impact of pre-salt rift topography on salt tectonics: a discrete-element modeling approach. Tectonics 38, 1466–1488. https://doi.org/10.1029/2018TC005174.
Quirk, D.G., Schødt, N., Lassen, B., Ings, S.J., Hsu, D., Hirsch, K.K., Von Nicolai, C., 2012. Salt tectonics on passive margins: examples from Santos, Campos and Kwanza basins. In: Alsop, G.I., Archer, S.G., Hartley, A.J., Grant, N.T., Hodgkinson, R. (Eds.), Salt Tectonics, Sediments and Prospectivity. Geol. Soc. Lond. Spec. Publ. 363, 207–244. https://doi.org/10.1144/SP363.10.
Ramberg, H., 1981. Gravity, deformation and the earth's crust, in theory, experiments and geological application (second edition). Academic Press, London.
Ritter, M.C., Rosenau, M., Oncken, O., 2018. Growing faults in the lab: insights into the scale dependence of the fault zone evolution process. Tectonics 37, 140–153. https://doi.org/10.1002/2017TC004787.
Rowan, M.G., Peel, F.J., Vendeville, B.C., 2004. Gravity-driven fold belts on passive margins. In: McClay, K.R. (Ed.), Thrust Tectonics and Hydrocarbon Systems. AAPG Memoir 482, 157–182. https://doi.org/10.1306/M82813C9.
Rowan, M.G., 2014. Passive-margin salt basins: hyperextension, evaporite deposition, and salt tectonics. Basin Res. 26, 154–182. https://doi.org/10.1111/bre.12043.
Rowan, M.G., 2018. The South Atlantic and Gulf of Mexico salt basins: crustal thinning, subsidence and accommodation for salt and presalt strataIn. In: McClay, K.R., Hammerstein, J.A. (Eds.), Passive Margins: Tectonics, Sedimentation and Magmatism. Geol. Soc. Lond. Spec. Publ. 476, 333–363. https://doi.org/10.1144/SP476.6.
Rowan, M.G., Peel, F.J., Vendeville, B.C., Gaullier, V., 2012. Salt tectonics at passive margins: geology versus models – Discussion. Mar. Petrol. Geol. 37, 184–194. https://doi.org/10.1016/j.marpetgeo.2012.04.007.
Rudolf, M., Boutelier, D., Rosenau, M., Schreurs, G., Oncken, O., 2016. Rheological benchmark of silicone oils used for analog modeling of short- and long-term lithospheric deformation. Tectonophysics 684, 12–22. https://doi.org/10.1016/j.tecto.2015.11.028.
Schultz-Ela, D.D., 2001. Excursus on gravity gliding and gravity spreading. J. Struct. Geol. 23, 725–731. https://doi.org/10.1016/S0191-8141(01)00004-9.
Spathoplous, F., 1996. An insight on salt tectonics in the Angola Basin, South Atlantic. In: McClay, K.R., Hammerstein, J.A. (Eds.), Passive Margins: Tectonics, Sedimentation and Magmatism. Geol. Soc. Lond. Spec. Publ. 11, 153–174. https://doi.org/10.1144/GSL.SP.1996.100.01.11.
Strozyk, F., Back, S., Kukla, P.A., 2017. Comparison of the rift and post-rift architecture of conjugated salt and salt-free basins offshore Brazil and Angola/Namibia, South Atlantic. Tectonophysics 716, 204–224. https://doi.org/10.1016/j.tecto.2016.12.012.
Tari, G., Jabour, H., 2013. Salt tectonics along the Atlantic margin of Morocco. In: Mohriak, W.U., Danforth, A., Post, P.J., Brown, D.E., Tari, G.C., Nemčok, M., Sinha, S.T. (Eds.), Conjugate Divergent Margins. Geol. Soc. Lond. Spec. Publ. 369, 337–353. https://doi.org/10.1144/SP369.23.
Valle, P.J., Gjelberg, J.G., Helland-Hansen, W., 2001. Tectonostratigraphic development in the eastern lower Congo basin, offshore Angola, west Africa. Mar. Petrol. Geol. 18, 909–927. https://doi.org/10.1016/S0264-8172(01)00036-8.
Vendeville, B., Cobbold, P.R., Davy, P., Brun, J.P., Chourkoune, P., 2012. Physical models of extensional tectonics at various scales. In: Coward, M.P., Dewey, J.F., Hancock, P.L. (Eds.), Continental Extension Tectonics. Geol. Soc. Lond. Spec. Publ. 28, 95–107. https://doi.org/10.1144/GSL.SP.1987.028.01.08.
Vendeville, B.C., Ge, H., Jackson, M.P.A., 1995. Scale models of salt tectonics during basement-involved extension. Petrol. Geosci. 1, 179–183. https://doi.org/10.1144/petgeo.1.2.179.
Warren, J.K., 2016. Flowing salt: halokinesis. In: Evaporites: A Geological Compendium. Springer, Cham, pp. 491–612. https://doi.org/10.1007/978-3-319-13512-0_6.
Warzitska, M., Závada, P., Jähne-Klingberg, F., Krzywiec, P., 2021. Contribution of Gravity Gliding in Salt-Bearing Rift Basins – A New Experimental Setup for Simulating Salt Tectonics under the Influence of Sub-salt Extension and Tilting. Solid Earth Discussions. https://doi.org/10.5194/se-2021-17 (Preprint).
Weijermars, R., 1986. Flow behaviour and physical chemistry of bouncing putties and related polymers in view of tectonic laboratory applications. Tectonophysics 124, 325–358. https://doi.org/10.1016/0040-1951(86)90208-8.
Westoby, M.J., Brasington, J., Glasser, N.F., Hambrey, M.J., Reynolds, J.M., 2012. Structure-from-Motion photogrammetry: A low-cost, effective tool for geoscience applications. Geomorphology 179, 300–314. https://doi.org/10.1016/j.geomorph.2012.08.021.
Zalán, P.V., Severino, M.C.G., Rigoti, C.A., Magnavita, L.P., Oliveira, J.A.B., Vianna, A. R., 2011. An entirely new 3-D view of the crustal and mantle structure of a South Atlantic passive margin – Santos. Campos and Espírito Santo Basins, Brazil. AAPG Search and Discovery Article #30177. http://www.searchanddiscovery.com/documents/2011/30177zalan/ndx_zalan.pdf.
Zwaan, F., Schreurs, G., Naliboff, J., Buiter, S.J.H., 2016. Insights into the effects of oblique extension on continental rift interaction from 3D analogue and numerical models. Tectonophysics 693, 239–260. https://doi.org/10.1016/j.tecto.2016.02.036.
Zwaan, F., Schreurs, G., Ritter, M., Santimano, T., Rosenau, M., 2018. Rheology of PDMS-Corundum Sand Mixtures from the Tectonic Modelling Lab of the University of Bern (CH). GFZ Data Services. https://doi.org/10.5880/fidgeo.2018.023.
Zwaan, F., Rosenau, M., Maestrelli, D., 2021. Digital image correlation data from analogue modelling experiments addressing the influence of basin geometry on gravity-driven salt tectonics at the Tectonic Modelling Lab of the University of Rennes (F). GFZ Data Services. https://doi.org/10.5880/fidgeo.2021.028.